JOURNAL OF APPLIED CRYSTALLOGRAPHY

ISSN 1600-5767

Received 12 December 2023
Accepted 22 April 2024

Edited by A. Borbély, Ecole National Supérieure des Mines, Saint-Etienne, France

This article is part of a collection of articles from the IUCr 2023 Congress in Melbourne, Australia, and commemorates the 75th anniversary of the IUCr.

**Keywords:** functional materials; structural science; structure–dynamic properties relationships.

# The master key: structural science in unlocking functional materials advancements

**Sebastian A. Suarez**[a,b]*

[a]DQIAyQF, FCEN-UBA, INQUIMAE-CONICET, Ciudad Universitaria, Pabellon II, Piso 3, Ciudad Autonoma de Buenos Aires, 1428, Argentina, and [b]Department of Plant Ecophysiology, Faculty of Biology, Adam Mickiewicz University, Uniwersytetu Poznańskiego 6, 61-614 Poznań, Poland. *Correspondence e-mail: sebastian.suarez@amu.edu.pl, seba@qi.fcen.uba.ar

From the historical roots of metalworking to the forefront of modern nanotechnology, functional materials have played a pivotal role in transforming societies, and their influence is poised to persist into the future. Encompassing a wide array of solid-state materials, spanning semiconductors to polymers, molecular crystals to nanoparticles, functional materials find application in critical sectors such as electronics, computers, information, communication, biotechnology, aerospace, defense, environment, energy, medicine and consumer products. This feature article delves into diverse instances of functional materials, exploring their structures, their properties and the underlying mechanisms that contribute to their outstanding performance across fields like batteries, photovoltaics, magnetics and heterogeneous catalysts. The field of structural sciences serves as the cornerstone for unraveling the intricate relationship between structure, dynamics and function. Acting as a bridge, it connects the fundamental understanding of materials to their practical applications.

## 1. Centuries of history

Functional materials (FM) have been instrumental in shaping human civilization throughout history. Renowned for their distinctive properties and capabilities, these materials have served as the cornerstones for numerous technological breakthroughs, propelling societies to thrive and evolve. The roots of FM trace back to ancient civilizations, where humans first harnessed the potential of naturally occurring materials (Hummel, 2004; Aizenberg & Levkin, 2020; Faustini *et al.*, 2018. A landmark example from prehistoric times is the discovery of fire and the utilization of quartz as a tool, marking the inception of FM (Norton, 2021). The advent of metals such as copper and bronze represented a significant leap forward in the realm of FM (Pandey *et al.*, 2023). The Bronze Age's development of metallurgy facilitated the creation of tools and weapons, further augmenting human capabilities (Grigoriev, 2021). The early experimentation with these materials laid the groundwork for subsequent innovations. Moving forward, the Middle Ages witnessed the rise of alchemy, a precursor to modern chemistry, driven by the pursuit of transforming base metals into noble ones and discovering the elixir of life. While rooted in mysticism and folklore, the endeavors of alchemists laid the foundation for comprehending the properties and transformation of materials (Szydło, 2022). The Renaissance marked a resurgence of scientific inquiry, leading to innovations in glassmaking and optics that birthed the microscope and telescope, expanding our understanding of the world and fostering scientific discovery. These advancements played a pivotal role in future investigations into the structure and

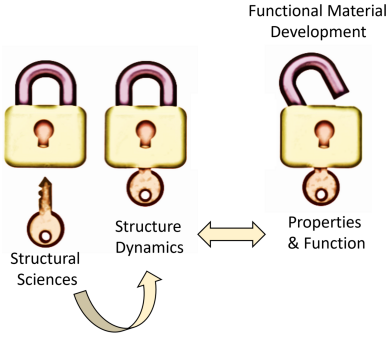


**Figure 1**
Centuries of history. Functional materials have consistently occupied a leading role in driving technological innovations of every era.

properties of materials (Richet, 2021; Špelda, 2019). Closer in time, the 18th and 19th centuries ushered in the Industrial Revolution, characterized by significant advancements in the manufacturing and utilization of FM. The discovery of electricity and subsequent developments in electrical conductors and insulators revolutionized technology (Heilbron, 2022). In the textile industry, innovations such as synthetic dyes and fibers had a profound impact on clothing and fashion (Zhang, Xia *et al.*, 2023). The late 19th century saw the emergence of materials science as a field, driven by the need for superior materials in various industries. The discovery of new functional materials, such as steel alloys and semiconductors, led to the development of telegraph and telephone networks, marking the birth of the electronics industry (Prescott, 2022). The 20th century witnessed an unprecedented surge in materials science and engineering. Discoveries like superconductors, along with advancements in polymers and composites, revolutionized industries from transportation to healthcare (Lim *et al.*, 2020). The atomic age brought forth both destructive and constructive consequences, leading to the development of nuclear materials and nuclear power for energy production (Zheng *et al.*, 2020; Wang, Li *et al.*, 2020; Xiang *et al.*, 2019). The mid-20th century marked the onset of the space age, where materials like titanium and advanced ceramics played crucial roles in spacecraft construction and space exploration (Dada *et al.*, 2023). Throughout these transformative periods, functional materials remained at the forefront of technological innovations, defining and shaping the trajectory of each era (Fig. 1).

## 2. The modern era. Structural characterization techniques

Today, functional materials continue to drive scientific and technological advancements (Preuss *et al.*, 2020; Xiao & Gu, 2020). Our ability to engineer and understand materials at the atomic and molecular levels has never been greater (Han *et al.*, 2022), and the historical journey of FM has paved the way for a promising future filled with innovations yet to be discovered (Azamal Husen, 2023; Shahed *et al.*, 2023). The structural sciences have a fundamental role in the development of materials, serving as the foundation for understanding and optimizing their properties and behaviors (Catlow, 2018; Taylor & Wood, 2019). By employing a wide range of analytical techniques and methodologies, these sciences provide insights into the atomic and molecular arrangements, crystal structures, and chemical compositions of materials (Freund *et al.*, 2023). On the one hand, the chemical composition of materials is a critical aspect that the structural sciences address (Fig. 2). Spectroscopic methods, like X-ray photoelectron spectroscopy (XPS) (Krishna & Philip, 2022), X-ray fluorescence (XRF) (Tsuji *et al.*, 2015) and multi-nuclear magnetic resonance (NMR) (Wei *et al.*, 2022), or scanning electron microscopy (SEM) with energy-dispersive X-ray spectroscopy (EDS) detectors (Abd Mutalib *et al.*, 2017), provide information about the elemental composition and chemical bonding in materials. X-ray absorption fine structure (XAFS) refers to how X-rays are absorbed by an atom at energies near and above the nuclear-level binding energies of the atom (Bunker, 2010). XAFS spectra are sensitive to factors such as formal oxidation state, coordination chemistry, and the arrangement of neighboring atoms in terms of distances, coordination numbers and species. Raman spectroscopy (Wang, Huang *et al.*, 2020) relies on the inelastic scattering of monochromatic light to analyze molecular vibrations and rotational modes. Also, terahertz spectroscopy explores the electromagnetic spectrum between microwave and infrared frequencies (Spies *et al.*, 2020; Neu, 2023).

On the other hand, the fundamental contribution of structural sciences is the elucidation of the atomic and molecular arrangements within materials (Fig. 2). Techniques like X-ray diffraction (XRD), neutron scattering and electron microscopy enable researchers to determine the precise arrangement of atoms and molecules in crystalline and amorphous materials (Liebschner *et al.*, 2019). This information is crucial for understanding how different materials interact with light, electricity and heat, laying the groundwork for developing materials with specific optical (Das *et al.*, 2020; Sanderson & Castelvecchi, 2023), electrical (Li, Cai *et al.*, 2023) and thermal properties (Atinafu *et al.*, 2023). Moreover, the field of structural sciences contributes significantly to the characterization of nanomaterials. With the growing interest in nanotechnology, the ability to determine the size, shape and distribution of nanoparticles within a material is paramount. Techniques such as transmission electron microscopy (TEM) (Li, Zhang & Han, 2023), scanning tunneling microscopy (STM) (Ko *et al.*, 2019) and atomic force microscopy (AFM) (Firestein *et al.*, 2020) offer unprecedented views of nanoscale structures. Modern TEM instruments are equipped with advanced detectors, such as aberration-corrected imaging and electron energy-loss spectroscopy, enabling the examination of defects, interfaces and nanostructures (Gao *et al.*, 2022).

Therefore, structural sciences are instrumental in understanding defects and imperfections in materials (Bourgeois *et al.*, 2020; Jia *et al.*, 2020). These imperfections can have a profound impact on the mechanical (Liu *et al.*, 2022), electrical (Bhaskar *et al.*, 2021; Neverov *et al.*, 2022) and optical (Akl & Hassanien, 2021) properties of materials.

Synchrotron radiation (SR) is essential for investigating functional materials. SR sources provide intense beams of X-rays and other electromagnetic radiation. Modern synchrotrons offer advanced FM beamlines equipped with monochromators and detectors that allow a wide range of experiments (Smieska *et al.*, 2023; Willmott, 2011). In the same vein, high-brightness MetalJet X-ray sources (powered by liquid-metal micro-jets) offer in-house laboratories a higher level of X-ray intensity and focus than traditional X-ray sources (Murrie *et al.*, 2020).

Finally, it is important to mention the contribution of neutron techniques (NTs). One of their primary benefits is their ability to provide precise information about the arrangement of atoms within a material (Boothroyd, 2020; Ridley & Kamenev, 2014). Unlike X-rays, neutrons have elastic interactions with condensed matter that occur at atomic nuclei. The scattering power is heavily dependent on individual nuclear properties, such as scattering length and cross section, which are randomly distributed throughout the periodic table, even among isotopes of the same element (Joseph, 2020). Neutrons are particularly useful in analyzing materials that contain both light and heavy elements. Additionally, neutron techniques are highly effective in studying the dynamic behavior of materials over a range of timescales, from hours to milliseconds. NTs can capture the movements and vibrations of atoms and molecules in real time (Hansen & Kohlmann, 2014; Goonetilleke & Sharma, 2021; Isnard, 2007). These techniques provide insight into reaction pathways, allowing for strategic synthesis planning, revealing intermediate steps and quantifying reaction kinetics. Moreover, the high penetration depth of thermal neutrons enables the analysis of complex sample environments. This is especially useful for studying phase transitions, magnetic properties and particle diffusion in materials, as explained below.

Computational methods have also emerged as powerful tools for characterizing functional materials, offering a cost-effective and efficient means to explore their properties and behavior (Wan *et al.*, 2023; Kalhor *et al.*, 2024). One of the most significant contributions of modeling and simulation techniques is their ability to predict novel materials with

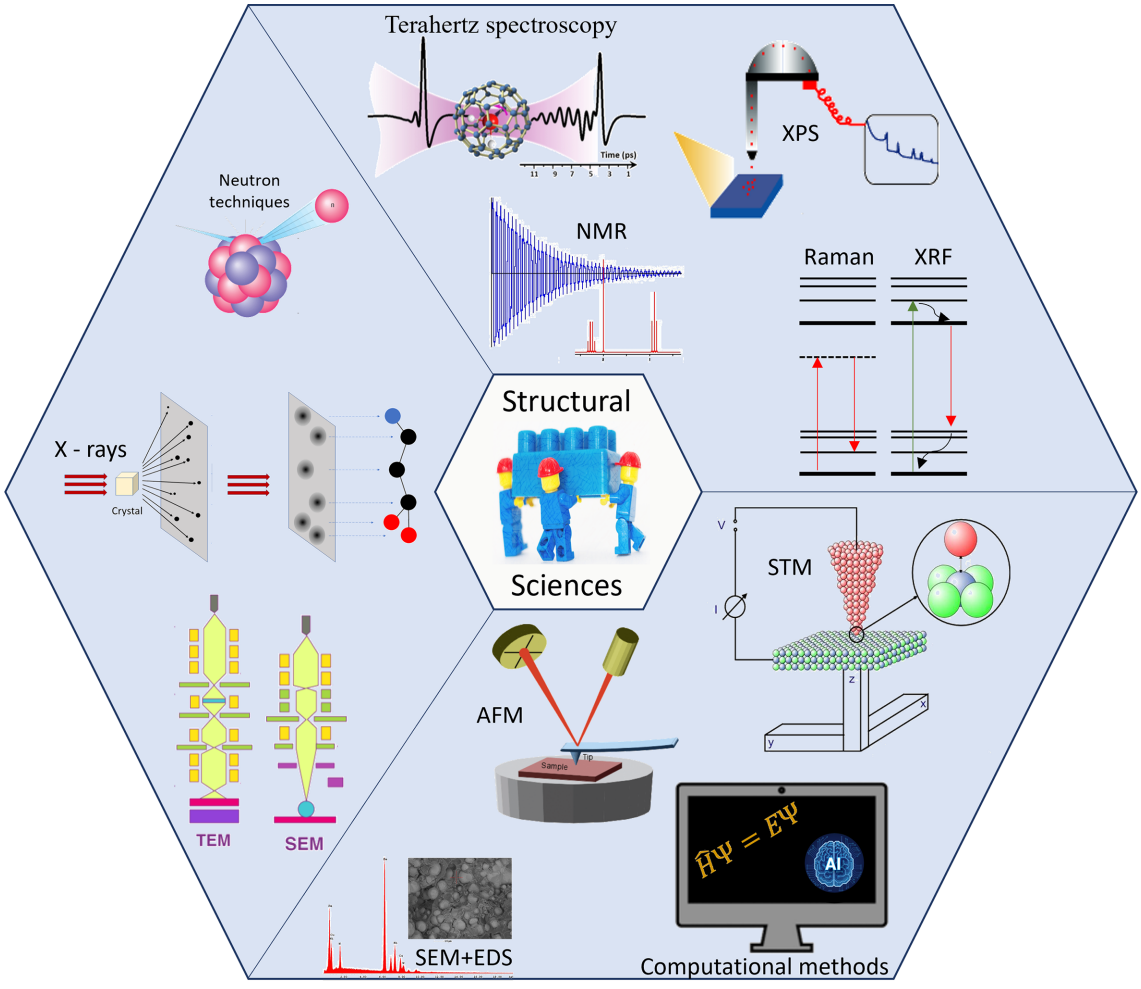


**Figure 2**
Conventional structural characterization techniques of functional materials.

desirable properties for specific applications (Todorović *et al.*, 2019; Merchant *et al.*, 2023). Crystal structure prediction (CSP) is the process of identifying the most thermodynamically stable crystal structure(s) that will form from a given molecule on the basis of its molecular structure (Woodley *et al.*, 2020; Cruz-Cabeza, 2016). Computational methods are used to search *ab initio* for the most stable crystal structure of a given molecule by evaluating the crystal energy landscape. The Cambridge Crystallographic Data Centre periodically assesses CSP methods through Blind Tests (https://www.ccdc.cam.ac.uk/discover/news/conclusions-of-the-7th-crystal-structure-prediction-blind-test/). Machine learning and artificial intelligence algorithms have also become essential tools in materials discovery. These techniques can process vast datasets and identify hidden patterns, enabling us to predict the properties of materials according to their chemical compositions and structures (Wang & Sun, 2019; Cheng *et al.*, 2022). This predictive capability accelerates the development of new materials with tailored properties, saving time and resources (Hsu *et al.*, 2022). Moreover, computational methods provide insights into atomic and molecular structures (Liu *et al.*, 2023; Hehn *et al.*, 2022). Another key contribution of computational methods is their ability to simulate material properties under different conditions. They can model the behavior of FM in response to various factors such as temperature, pressure and external stimuli (Asrafusjaman *et al.*, 2023; Kalhor *et al.*, 2024). These simulations provide valuable insights into how materials perform in real-world applications (Islam & Hossain, 2020). Finally, computational methods can simulate the properties of materials with different compositions and structures to identify the most suitable configurations for specific applications (Borgmans *et al.*, 2021; Baird *et al.*, 2022).

## 3. . . . and beyond. *In situ* monitoring of structural evolutions during reactions

In the past decade, experimental techniques have transformed our ability to understand and characterize dynamic processes in functional materials that play a crucial role in their performance. These techniques, which include imaging, spectroscopy and microscopy, enable researchers to investigate materials *in situ* at the atomic and molecular levels, uncovering their electronic (Zhao *et al.*, 2022), optical (Zhang *et al.*, 2022) or mechanical properties (Akkuratov *et al.*, 2022). Furthermore, *in situ* techniques allow scientists to monitor these transitions, providing insights into the underlying mechanisms.

One of the revolutionary tools that has significantly contributed to this understanding is the X-ray free-electron laser [XFEL; Fig. 3(A)]. Traditional X-ray sources, such as synchrotrons, had limitations in terms of brightness and pulse duration. XFELs overcome these limitations by producing extremely intense and ultra-short X-ray pulses. XFELs have brought about a paradigm shift in our ability to investigate the atomic and molecular structures of functional materials (Asakura *et al.*, 2020; Huang *et al.*, 2021; Jaeschke *et al.*, 2020). This level of detail is invaluable in understanding the fundamental structural aspects that govern the properties of materials and behavior. Finally, XFELs have proven instrumental in studying dynamic processes in real time (Holstad *et al.*, 2023; Choi *et al.*, 2022).

Three-dimensional electron diffraction (3DED) is another powerful technique that has significantly advanced our ability to develop new FM [Fig. 3(B)] (Yonekura *et al.*, 2023; Saha *et al.*, 2022; Gruene *et al.*, 2021; Klar *et al.*, 2023). Gemmi *et al.* (2019) suggested the name '3DED' as an umbrella term for several techniques that collect reflection intensities in three-dimensional reciprocal space through an electron diffraction experiment. Traditional electron diffraction techniques, while providing valuable structural information, are typically limited to two-dimensional projections. In contrast, 3DED allows researchers to capture a complete three-dimensional crystal structure, providing a holistic view of the arrangement of atoms (Kolb *et al.*, 2007). This information is critical for understanding how the atomic structure influences the properties and functionality of materials (Frolov *et al.*, 2020). Moreover, *in situ* 3DED combines electron microscopy with

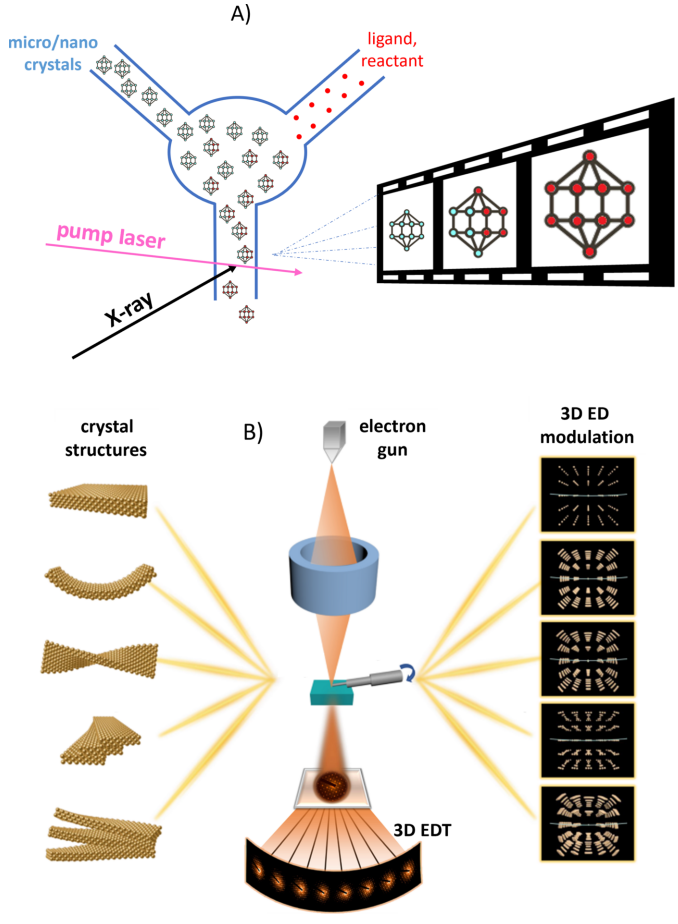


**Figure 3**
(A) The 'mix-and-inject' time-resolved serial crystallography strategy takes advantage of the small crystals that can be analyzed with an XFEL. (B) Schematic drawing of representative crystal structures and their corresponding modulated diffraction spots in reciprocal space for a three-dimensional electron diffraction experiment. Panel (B) adapted from Ai *et al.* (2022) under a Creative Commons Attribution 4.0 International License, https://creativecommons.org/licenses/by/4.0/.

crystallography and offers unique insights into the dynamic behavior and structural transformations of materials at the atomic and nanoscale levels. One of the primary ways in which *in situ* 3DED contributes to the development of new functional materials is by offering a dynamic view of phase transitions and crystal growth (Batuk *et al.*, 2023; Broadhurst *et al.*, 2020; Karakulina *et al.*, 2018; Wu *et al.*, 2022). In the same vein, precession electron diffraction tomography (PEDT) combines the principles of electron diffraction and tomography (Day *et al.*, 2022; Boullay *et al.*, 2013). One of the primary advantages of PEDT is its ability to resolve complex crystal structures, even in materials with multiple phases or high levels of defects (Palatinus *et al.*, 2019). This capability is crucial to precisely determine the orientations and locations of individual grains, crystal defects and interfaces within a material (Rauch *et al.*, 2008).

## 4. Looking to the future. Unlocking the potential of structured functional materials, a path to enhanced properties

This article provides an overview of the *Microsymposium A040: Crystal Structure of Functional Materials*, held during the 26th Congress and General Assembly of the International Union of Crystallography (IUCr) in Melbourne in 2023. This work intends to encapsulate the insights shared by the invited speakers, the valuable contributions from oral presentations and the diverse array of poster presentations within the microsymposium. It also includes several other relevant and recent papers. While the applications of FM are very diverse, this section explores their structures, properties and underlying dynamic mechanisms driving exceptional performance in the fields of batteries, optoelectronics, magnetics and heterogeneous catalysts.

### 4.1. Battery materials

Metal-ion batteries play a pivotal role in the contemporary shift from fossil fuels to renewable energy, contributing to a more sustainable planet through the innovation of ingeniously designed materials. These batteries, featuring metals such as lithium, zinc, magnesium, calcium, potassium and sodium, serve as promising candidates for energy storage devices, offering enhanced performance compared with current battery technologies (Abakumov *et al.*, 2020). Furthermore, the solid-state battery, featuring the substitution of conventional liquid electrolytes with solid-state electrolytes, stands out as one of the most promising energy storage systems, capable of demonstrating both high safety and high energy density concurrently (Chen, Shen *et al.*, 2022). In addition, the development of all-solid-state batteries (ASSBs) critically depends on the fundamental understanding of the electrochemical reaction mechanisms and the synchronously occurring degradation causes. In this context, synchrotron X-ray computed tomography (SX-CT) can visualize the internal structure of a sample, making it well suited for the examination of concealed interfaces. For instance, Sun *et al.* (2022) revealed the emergence of a complex and varied reaction interphase region, illustrated as the green region in Fig. 4, following the cycling of $Li_{10}SnP_2S_{12}$-based ASSBs. The 3D volume rendering of the $Li_{10}SnP_2S_{12}$ solid electrolyte (LSPS SE) in Fig. 4(A) vividly portrays its transformation into a bowl-like structure with evident surface cracks (depicted by white isolines). To highlight alterations within the LSPS, a sectional plane [demarcated by the green rectangle in

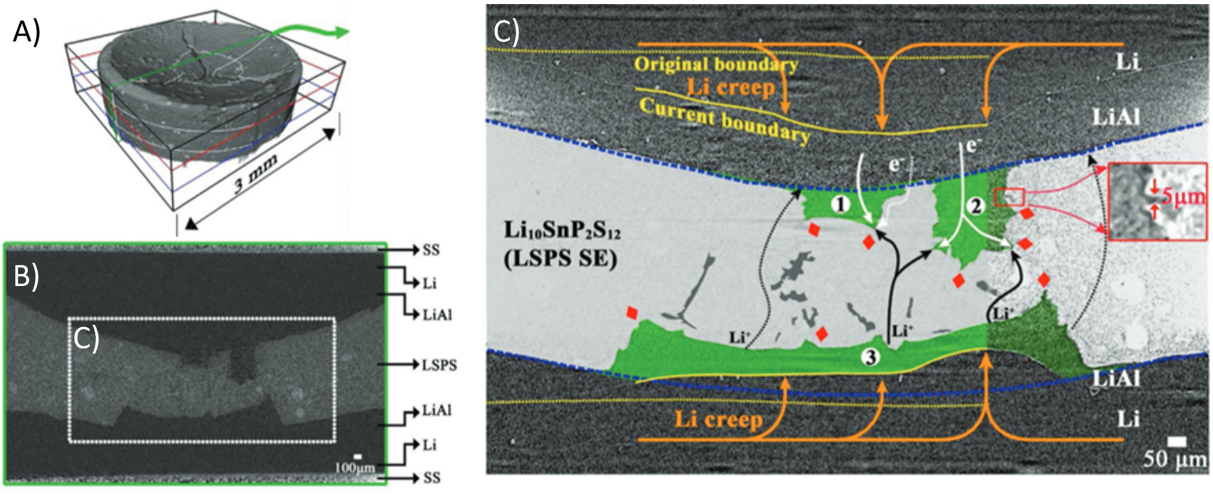


**Figure 4**
Results from SX-CT characterization are presented as follows: (A) A 3D volume rendering of the LSPS SE. (B) The cross section chosen from (A) is highlighted by a green rectangle. An inset white dotted rectangle indicates the region featured in (C). (C) A magnified view of the selected cross section of the LSPS SE. The yellow dotted and solid lines represent the original and current Li|LiAl interfaces, respectively. The LiAl|LSPS interface is delineated by blue dashed lines. Regions marked (1), (2), and (3) in green signify the electrochemically generated interphase. Red diamonds mark crack tips, while the red rectangle indicates a crack size of approximately 5 μm. Irregular dark-gray regions denote the as-formed cracks. Orange arrow lines depict the direction of Li creep. Both solid and dotted black and white arrow lines suggest potential pathways for Li ions and electrons during electrochemical cycling. Adapted, with permission, from Fig. 2 of Sun *et al.* (2022), copyright 2022 Wiley-VCH GmbH.

Fig. 4(A)] is chosen, as demonstrated in Fig. 4(B). A closer examination is provided in Fig. 4(C), revealing several notable features (Sun *et al.*, 2022):

(i) The LSPS layer appears to sag towards the bottom electrode layer, forming the bowl-like shape observed in Fig. 4(A) (marked by the blue dashed lines).

(ii) Multiple low X-ray absorption interphase regions manifest at the LiAl|SE interface [designated as regions (1), (2), and (3)], contributing to the surface cracks depicted in Fig. 4(A).

(iii) The boundary lines between the Li metal and LiAl alloy seem to deform towards the LSPS layer (contrasting yellow solid lines with yellow dotted lines).

(iv) Crack and fissure structures develop within the contorted region of the LSPS solid electrolyte (depicted as dark-gray regions).

In addition, heterogeneous damage in metal-ion batteries has been analyzed (Xu *et al.*, 2019; Santos *et al.*, 2023; Lin *et al.*, 2021; Li, Sharma *et al.*, 2022). Utilizing a combination of advanced synchrotron X-ray tomography analysis and microstructure-resolved computational modeling, Xu *et al.* (2019) studied the heterogeneous electrochemistry and mechanics within a composite cathode in commercial batteries. The focus was on examining the spatially and temporally evolving heterogeneous damage, spanning from the macroscopic level of composites down to individual particles. Within an extensive dataset comprising over a thousand $LiNiMnCoO_2$ (NMC) particles, particle fracture and interfacial debonding phenomena are identified (Fig. 5). The degree of particle fracture is notably higher in the region near the separator compared with that toward the current collector. A similar distribution is observed for interfacial debonding, indicating that particles near the separator tend to be more detached from the conductive network [Fig. 5(B)]. This interfacial damage hinders electron conduction, resulting in substantial capacity loss and polarization in batteries.

Moreover, the formation of extensive cracks in Ni-rich cathode secondary particles plays a pivotal role in long-term performance degradation. Employing *in situ* scanning electron microscopy, Cheng *et al.* (2021) recently elucidated the dynamic morphological changes within an individual $LiNi_{0.8}Mn_{0.1}Co_{0.1}O_2$ (NMC-811) secondary particle embedded in a cathode blend during electrochemical cycling. Under normal cycling conditions with a cutoff voltage of 4.1 V, only a minimal number of cracks appear in the particle. However, when the sample is subjected to extreme working conditions with an increased cutoff voltage of 4.7 V, several cracks are unmistakably generated in the core region. In Fig. 6(A), pristine NMC-811 secondary particles exhibit a densely packed arrangement, showcasing a well defined layered structure conducive to fast Li-ion diffusion channels. The structure model corroborates the retention of the layered phase [Fig. 6(B) and 6(C)], with brighter dots corresponding to metal atoms evident in the accompanying high-angle annular dark-field scanning transmission electron microscopy (HAADF-STEM) (Zhang *et al.*, 2020) image. However, after ten charge–discharge cycles, noticeable dendrite-shaped cracks emerge from the particle's center, flowing along grain boundaries [Fig. 6(D)], consistent with *in situ* SEM results (Cheng *et al.*, 2021). To glean structural insights around these cracks, atomic-resolution HAADF-STEM analysis was performed [Fig. 6(E)]. A distinct atomic arrangement at the

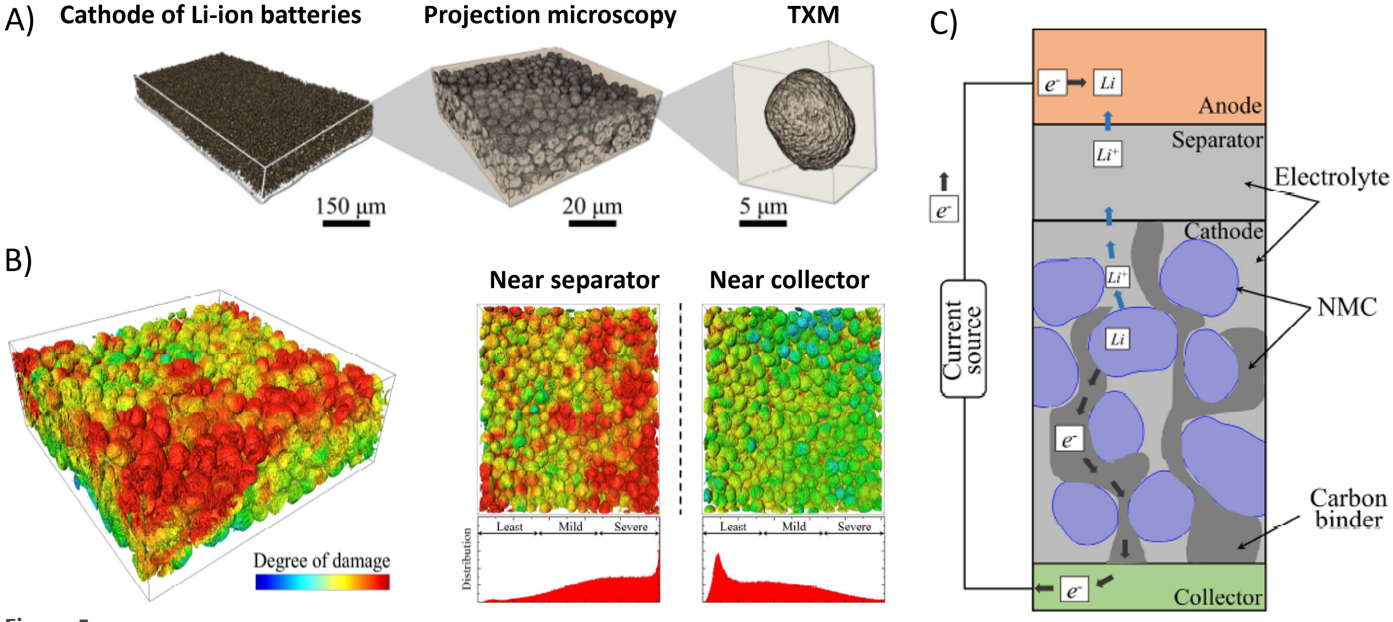


**Figure 5**
(A) Tomographic data from the composite film down to a single active particle in an NMC cathode of Li-ion batteries. (B) The 3D profile of particle fracture in a selected regime of 150 × 150 × 40 μm, showing the spatially heterogeneous damage, including particle fracture and interfacial debonding, in the NMC cathode after 10 cycles with the cyclic rate of 5 C. NMC particles are color-coded according to the degree of damage – red represents the severely fractured particles and blue represents the least damaged particles. (C) Sketch of the working principle of a half-cell composed of an NMC cathode and a Li metal anode. Adapted from Xu *et al.* (2019) with permission from Elsevier.

side surface of the cracks is observed compared with the inner region.

The structure model is presented in Fig. 6(F), revealing a structural reconstruction layer approximately 10 nm thick—a consistent finding with previous reports for polycrystalline Ni-rich layered oxides. From this perspective, phase transformation emerges as a plausible explanation for crack propagation. These cracks then propagate radially along the grain boundaries, eventually reaching the particle's surface. Notably, the process of crack propagation follows a recurring 'grow–stagnate–grow' pattern during charge–discharge cycling. This direct *in situ* investigation provides a comprehensive map of crack evolution in the cathode, offering insights into the early stages of electrochemical cycling.

As mentioned earlier, sodium-ion batteries (SIBs), leveraging readily available sodium reserves and employing reaction mechanisms akin to lithium-ion batteries, are considered a promising large-scale energy storage technology for the next generation. Recently, the creation of superstructured mesocrystals utilizing numerous inherent molecular interactions to enhance the reversibility of sodium-ion batteries was reported (Qiu *et al.*, 2021). Soft structures found in nature, such as supercoiled DNA and proteins, can arrange themselves into intricate hierarchical configurations through various noncovalent molecular interactions. The quest for discovering novel categories of natural building blocks that can facilitate the formation of extensive hierarchical structures has proven challenging. Qiu *et al.* (2021) presented the systematic construction, from the ground up, of a hierarchical metal–phenolic mesocrystal with an ordered quaternary structure based on a self-assembled small planar natural phenolic molecule (ellagic acid, EA) with bismuth ions ($Bi^{3+}$) (Fig. 7). This self-assembly process occurs at different length scales in a carefully controlled spatiotemporal manner. Coordination complexes based on phenolic compounds form supramolecular threads, which then organize into tertiary nanoscale filaments. Finally, these filaments pack together to form quaternary mesocrystals (Fig. 7). Remarkably, the hierarchically ordered structures persist even after undergoing thermal conversion into a metal–carbon hybrid framework. The potential applications of this hierarchical structuring of natural polyphenols are expected to be widespread.

Furthermore, Chen, Xiao *et al.* (2022) conducted nanoengineering to introduce *in situ* anchored bismuth dots into modified porous carbon, resulting in enhanced sodium-ion storage capabilities. A designed composite featuring uniformly anchored bismuth dots on a three-dimensional porous carbon matrix (Bi@MC) has been successfully synthesized through a straightforward KOH-assisted annealing approach and applied in SIBs. This innovative design effectively addresses the inherent low initial Coulombic efficiency challenge associated with bismuth-based anodes, while density functional theory (DFT) calculations confirm that KOH plays a crucial role in preventing bismuth dot aggregation and ensuring an even distribution. The KOH-modified carbon demonstrates enhanced adsorption/desorption capabilities for sodium ions compared with unmodified carbon, facilitating greater interaction with the carbon surface of the Bi@MC electrode and promoting beneficial subsequent alloying reactions between bismuth and sodium ions. This modification reduces irreversible sodium trapping, leading to exceptional cycle stability. Then, the XRD pattern depicts the gradual

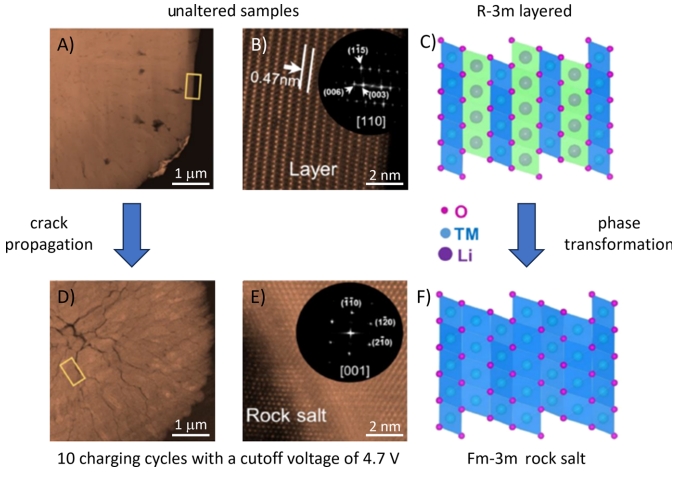


**Figure 6**
Characterization through *ex situ* HAADF-STEM was conducted on (A) and (B) unaltered samples and (D) and (E) samples subjected to 10 charging cycles with a cutoff voltage of 4.7 V. The insets of panels (B) and (E) display the respective fast Fourier transformation patterns, while the structural models for the pristine and charged states are illustrated in panels (C) and (F), respectively. Adapted from Cheng *et al.* (2021). Copyright 2021 American Chemical Society.

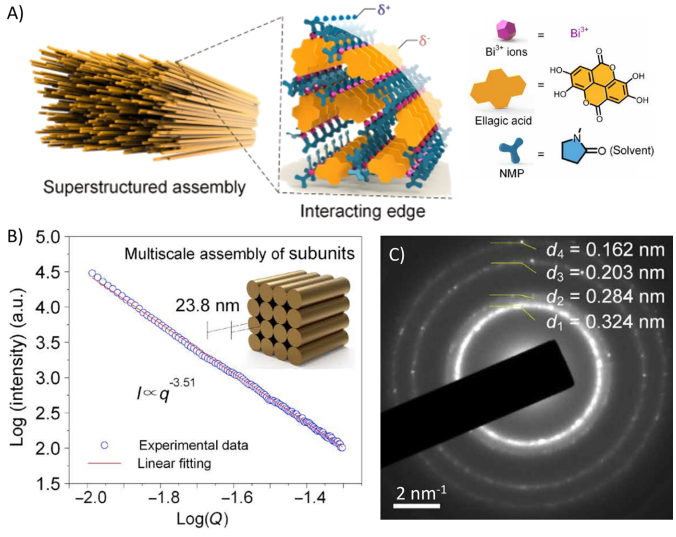


**Figure 7**
Supramolecular hierarchical assembly of Bi–EA mesocrystals, orchestrated in a spatiotemporally controlled fashion through multiple inherent molecular interactions. (A) Representation of the hierarchical assembly process, showcasing the structured Bi–EA mesocrystals formed through various molecular interactions operating on different length scales. (B) Analyzed small-angle X-ray scattering data of the Bi–EA mesocrystals, accompanied by a schematic depiction outlining the multiscale structure from filaments to the mesocrystal. (C) Selected-area electron diffraction pattern of a Bi–EA mesocrystal. Adapted from Qiu *et al.* (2021) under a Creative Commons Attribution 4.0 International License, https://creativecommons.org/licenses/by/4.0/.

transformation of $Na_3Bi$ to NaBi and Bi in a stepwise manner [see Fig. 8(A)]. Notably, the strength of the (012) plane in Bi (27°) steadily decreases within the voltage range of 1.6–0.65 V, while NaBi (100) (27°) and (101) (25.7 and 31.9°) emerge at 0.65 V. In the initial plateau spanning 0.65–0.47 V, the alloying reaction of Bi and Na (Bi + Na → NaBi) is confirmed through observable changes in the Bi and NaBi peaks. Subsequently, within the measured potential window of 0.5–0.1 V, a further sodiation process converts NaBi into the $Na_3Bi$ phase (peaks at 20.6, 32.8 and 33.6°). Throughout the charging process, $Na_3Bi$ undergoes gradual and reversible decomposition into NaBi and Bi within voltage regions of 0.61–0.77 V and 0.77–1.5 V, respectively. A schematic diagram illustrating the electrochemical mechanism of the Bi@MC electrode during the sodiation/desodiation process is presented in Fig. 8(B).

Finally, three recent studies discussed innovative advancements in the synthesis and application of FM for the enhancement of charge carrier transport in electrochemical devices. Numerical simulations were employed to quantitatively analyze the impact of various electrode parameters on electrochemical properties in high-energy $LiNi_{0.8}Mn_{0.1}Co_{0.1}$ (NMC811)//graphite systems. The insights gained from simulations inform discussions on recent experimental endeavors aimed at designing electroactive materials and electrode architectures across multiple length scales. Nanostructuring is identified as a strategy to enhance local mass transport and stabilize interfaces at the particle level, while microstructuring establishes efficient pathways for charge carriers at the electrode level (Ju *et al.*, 2023). A tight iterative approach combining structural engineering, characterization and simulation is deemed essential for accelerating the comprehension of deficiencies in current electrode designs and identifying potential routes for optimizing electrodes in the pursuit of next-generation fast-charging batteries. Moreover, Hyun *et al.* (2022) reported the implementation of a porosity-graded 3D nanostructure, underscoring the critical importance of structurally designing electrodes for cutting-edge energy storage devices. The integration of a density-graded 3D composite electrode with a porosity-graded current collector offers a compelling avenue for effectively enhancing rate capability. Four distinct types of current collectors with varying porosity gradients were established through meticulous pore analysis using 3D imaging techniques, demonstrating a proof-of-concept approach. Electropolishing, conducted under non-equilibrium conditions, emerged as a promising avenue for facile modification of pore networks within intricate nanostructures. This outcome validates the success in mitigating polarization, enhancing Li-ion diffusivity and reducing charge carrier transport resistance through precise adjustments of porosity and density gradient levels. Considering these density gradients, the development of electrodes with optimal geometries characterized by low tortuosity and optimized porosity holds the potential to realize swift and stable energy storage devices in the future. The concept of density gradient control in a composite electrode with an integrated 3D porosity-graded current collector is proposed as an electrode platform technology for diverse energy applications that necessitate the optimization of intricate transport challenges. Lastly, the engineering of functional bismuth-based chalcogenides emerges as a novel, effective and general approach to overcoming aggregation issues in metal anodes with low melting points, offering significant potential for advanced battery applications (Li, Yang *et al.*, 2023). However, synthesizing nanosized Bi structures poses a significant challenge as the low melting point of Bi makes it prone to aggregation into large ingots. Recently, a thin $Bi_4Se_3$ coating layer, combined with N-doped carbon, was introduced onto Bi nanospheres through an *in situ* selenization process to chemically confine their overgrowth. The favorable electrochemical performance was attributed to the thin and uniform $Bi_4Se_3$ and N-doped carbon coating layer, which not only alleviates volume expansion during electrode cycling but also accelerates K-ion diffusion kinetics. Moreover, the $Bi_4Se_3$ coating layer exhibited a reversible conversion/alloying mechanism, leading to unique final discharged products of $K_3BiSe_3$ and $K_3Bi$ (Fig. 9) which contribute to improved discharge capacity and superior cycle properties. The developed approach effectively addresses overgrowth issues in bismuth anodes and holds promise for mitigating challenges in other metal anodes with low melting points in advanced battery applications.

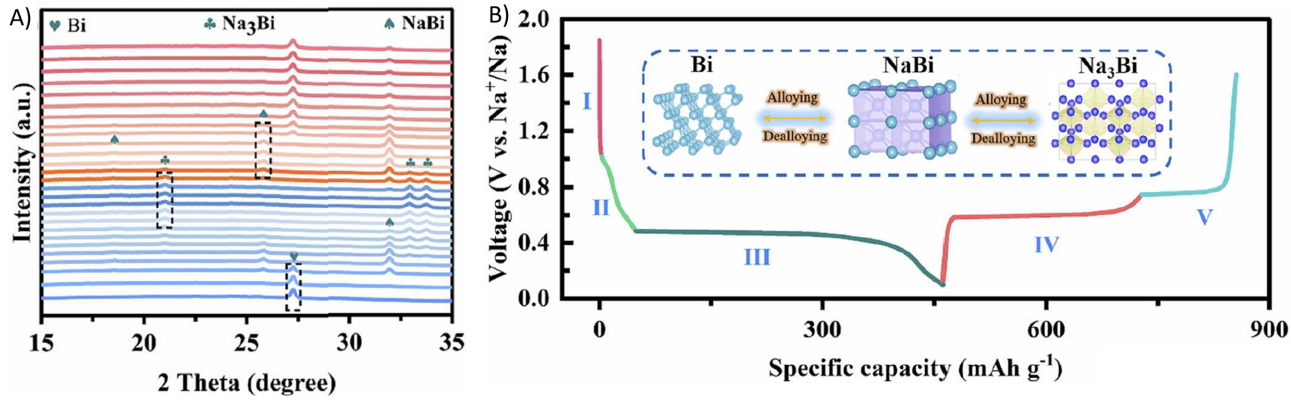


**Figure 8**
(A) *In situ* XRD patterns and the accompanying contour image of the Bi@MC electrode throughout the initial cycle. (B) Diagram depicting the electrochemical mechanism of the Bi@MC electrode during the sodiation/desodiation process. Adapted from Chen, Xiao *et al.* (2022) with permission from the Royal Society of Chemistry.

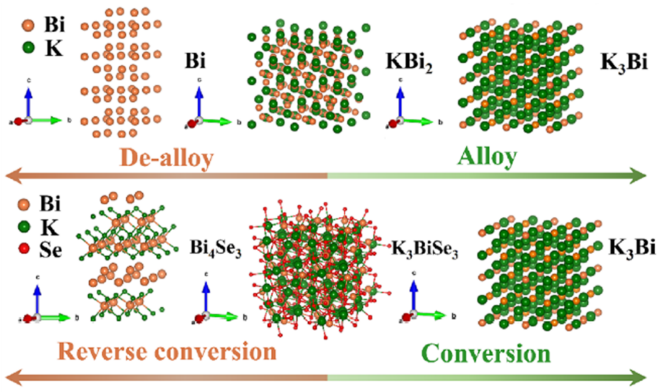


**Figure 9**
Diagram of alloying reaction and conversion reaction of thin $Bi_4Se_3$ combined with a N-doped carbon coating layer constructed on a Bi nanospheres electrode. Reproduced from Li, Yang *et al.* (2023) with permission from Elsevier.

No doubt these recent advances will help to optimize the design of energy storage materials, leading to improvements in battery performance, capacity and lifespan.

### 4.2. Magnetic materials

The advent of 2D magnets, a previously absent category in the realm of functional materials, holds great promise for advancing next-generation information technology (Jiang *et al.*, 2021; Li, Li *et al.*, 2021). Various types of 2D intrinsic magnetic materials were recently reported, encompassing binary transition metal halides, chalcogenides, carbides, nitrides, oxides, borides, silicides, MXenes, ternary transition metal compounds, f-state magnets, p-state magnets and organic magnets. The atomic thinness of 2D layers facilitates strong tunability through strain, intercalation, external fields (electronic, optical and magnetic), interfacial interaction, defects and functional groups (Jiang *et al.*, 2021).

In this context, the research team headed by Professor Zhang has extensively investigated strong magnets with ordered structures (Zhang, Zhang & Zhang, 2023; Zhang & Zhang, 2022). In 2021, by crafting $Nd_2Fe_{14}B/\alpha$-Fe gradient nanostructures, a unique phenomenon of directional magnetization reversal was unveiled, initiating from larger grains and progressing toward smaller ones (Lou *et al.*, 2021). This distinctive directional magnetization reversal yields an uncommon combination of elevated magnetization and substantial coercivity. Consequently, it results in an unprecedentedly high energy density of 26 MGOe for isotropic permanent magnetic materials, surpassing that of its gradient-free counterpart by approximately 50%. Moreover, Li, Lou *et al.* (2022) introduced an experimental strategy involving temperature-gradient-assisted self-assembly, enabling the creation of 3D macroscopic ordered nanocomposites with varying gradients in grain size, constituent content and crystal orientation [Fig. 10(A)]. The resulting $\alpha$-Fe/$Pr_2Fe_{14}B$ ordered nanostructure, featuring reverse gradients in both grain size and $\alpha$-Fe content [Fig. 10(B)–10(E)], demonstrates a remarkable energy density of approximately 25 MGOe for isotropic $\alpha$-Fe/$Pr_2Fe_{14}B$ systems. This value is approximately 130% higher than that of its disordered counterpart [Fig. 10(F)]. The atypical magnetization reversal is attributed to the ordered arrangement of grain sizes within the gradient material, where larger grains exhibit a lower reversal field compared with their smaller counterparts. There is no doubt that the formation of ordered nanostructures presents an alternative approach to developing high-performance permanent magnet materials.

In addition, the role of external stimuli in engineering magnetic phases and real-time spin dynamics was recently studied. Specifically, the spin-resolved density functional theory calculations on 2D magnetic hexagonal transition-metal oxide alloys were performed (Bandyopadhyay *et al.*, 2022). Various alloy patterns were explored, revealing distinct magnetic phases in each pattern which lead to a stable ferromagnetic ground state contingent upon the pattern selected. Janus functionalization was employed to modulate the magnetic nature of the system, transitioning it from a ferromagnetic to an antiferromagnetic state. To exert further control over spin dynamics, an ultrafast laser pulse was applied to the Janus systems, allowing for an exploration of the transition process from antiferromagnetic to ferromagnetic states. Additionally, the introduction of strain and electric fields to the Janus alloys enabled the fine-tuning of the structure–property relationship within the 2D layers, facilitating the achievement of desired spin arrangements.

The identification of van der Waals (vdW) magnets marked a transformative development in condensed matter physics and spintronic technologies. Using the computational methods described in Section 2, tuning of magnetic anisotropy in two-dimensional metal–semiconductor Janus van der Waals heterostructures was studied (Bandyopadhyay *et al.*, 2021). This investigation demonstrates that the diverse array of interface formations in Janus or pure metal–semiconductor-based van der Waals heterostructures provides an avenue for exploring and modifying spin–orbit and ligand–metal interactions. This enables the precise adjustment of magnetic anisotropy and diverse spin symmetries in these systems. Nevertheless, the functionality of active spintronic devices utilizing vdW ferromagnets is currently constrained to cryogenic temperatures, posing a barrier to their more widespread practical applications. In 2023, at least three studies made progress in developing Fe–Ge–Te systems that operate at room temperature (r.t.). In January, Zhao *et al.* (2023) showed the reliable operation of lateral spin-valve devices at r.t., employing the vdW itinerant ferromagnet $Fe_5GeTe_2$ in heterostructures with graphene. The spintronic properties of $Fe_5GeTe_2$ at r.t. were characterized at the interface with graphene, revealing a negative spin polarization. Through lateral spin-valve and spin-precession measurements, the authors gained unique insights into the spin dynamics at the interface, uncovering multidirectional spin polarization (Fig. 11). DFT calculations, coupled with Monte Carlo simulations, elucidate significantly canted Fe magnetic moments in $Fe_5GeTe_2$ and confirm the presence of negative spin polarization at the interface (Zhao *et al.*, 2023). A few months later, Lv *et al.*, (2023) established the successful large-area

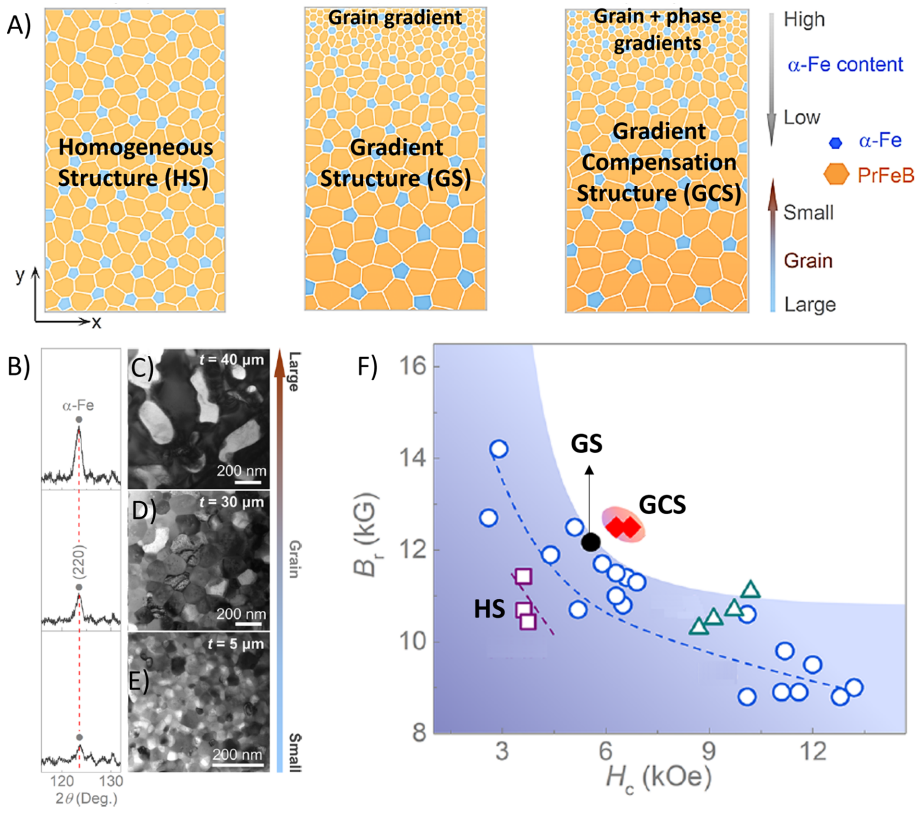


**Figure 10**
(A) Schematic representations illustrate $\alpha$-Fe/$Pr_2Fe_{14}B$ homogeneous structure (HS), gradient structure (GS) characterized by spatial variation in grain size, and gradient compensation structure (GCS) featuring reverse gradient variations in both grain size and $\alpha$-Fe content. All designed nanostructures maintain a consistent 20% $\alpha$-Fe composition. (B) A gradient variation in the crystal orientation of $Pr_2Fe_{14}B$ and $\alpha$-Fe phases can be achieved. The crystal orientations [110] for the $\alpha$-Fe phase weaken gradually as indicated by the decline in their corresponding diffraction peak intensity, accompanied by a decrease in grain size simultaneously. (C)–(E) Cross-sectional TEM images showing the mentioned grain size. (F) Remanence ($B_r$) and coercivity ($H_c$) values are presented for representative isotropic $\alpha$-Fe/$Pr_2Fe_{14}B$ nanocomposite magnets prepared using different methods. Adapted with permission from (Li, Lou *et al.*, 2022). Copyright 2022 American Chemical Society.

growth of $Fe_{5-x}GeTe_2$/graphene heterostructures through the vdW epitaxy of $Fe_{5-x}GeTe_2$ on epitaxial graphene. Structural analysis verifies the formation of a continuous vdW heterostructure film, characterized by a well defined interface. Magnetic and transport investigations demonstrate the persistence of ferromagnetic order well above 300 K, accompanied by a perpendicular magnetic anisotropy. Furthermore, the epitaxial graphene on silicon carbide [SiC(0001)] continues to exhibit high electronic quality (Lv *et al.*, 2023). Finally, at the end of the year, Li, Zhu *et al.* (2023) demonstrated the efficient switching of perpendicular magnetization in the vdW ferromagnet $Fe_3GaTe_2$ at r.t. (Curie temperature ~340 K) within an $Fe_3GaTe_2$/Pt bilayer using spin–orbit torques (SOTs) with a relatively low current density ($1.3 \times 10^7$ A cm$^{-2}$). The high SOT efficiency surpasses those observed in Pt-based heavy metal/conventional ferromagnet devices. These findings, showcasing r.t. vdW ferromagnet switching via SOTs, provide a crucial foundation for advancing spin-based logic and neuromorphic computing applications. However, an in-plane magnetic field is still required to break the in-plane symmetry for deterministic switching in our SOT devices, which is challenging for device integration.

Going one step further, understanding the behavior of materials in ultrafast magnetic storage devices will pave the way for improved data storage technologies. For example, the potential of manipulating spin in antiferromagnetic materials holds significant promise in antiferromagnetic opto-spintronics.

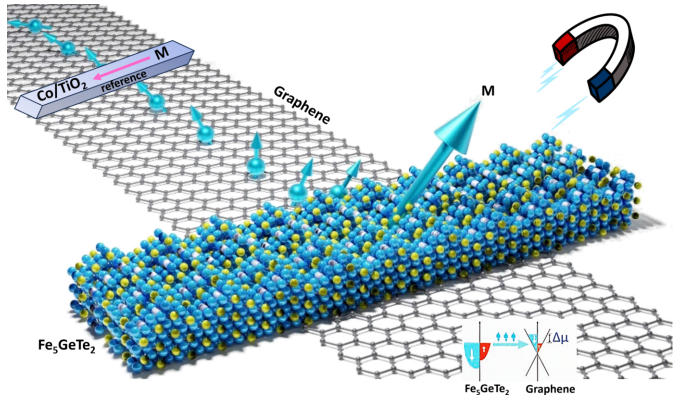


**Figure 11**
Diagram depicting a spin-valve device featuring $Fe_5GeTe_2$ on a graphene channel alongside a reference Co/$TiO_2$ electrode. The inset at the bottom right provides a schematic illustration of spin injection from $Fe_5GeTe_2$ into the graphene channel through the van der Waals gap, resulting in a non-equilibrium spin accumulation $\Delta\mu$ in graphene. Adapted from Zhao *et al.* (2023) under a Creative Commons Attribution 4.0 International License, https://creativecommons.org/licenses/by/4.0/.

While laser pulses have been known to induce a transient ferromagnetic state in antiferromagnetic metallic systems, this phenomenon has not been demonstrated in 2D antiferromagnetic semiconductors and related vdW heterostructures. In this regard, employing state-of-the-art real-time time-dependent density functional theory, the dynamics of optically induced interlayer spin transfer on 2D vdW heterostructures with ferromagnetic $MnS_2$ and antiferromagnetic MXenes as prototypes were investigated. The results revealed substantial spin injection and interfacial atom-mediated spin transfer from $MnS_2$ to $Cr_2CCl_2$ induced by laser pulses, providing the first demonstration of a transient ferromagnetic state in semiconducting antiferromagnetic–ferromagnetic heterostructures during photoexcited processes (Li, Zhou *et al.*, 2022). Applying a comparable method, an ultrafast laser pulse can prompt a nonmagnetic $MoSe_2$ monolayer interfaced with vdW ferromagnetic $MnSe_2$ to transition into a ferromagnetic state. The findings indicate that the momentary ferromagnetism observed in $MoSe_2$ originates from the immediate ultrafast interlayer spin transfer from Mn to Mo

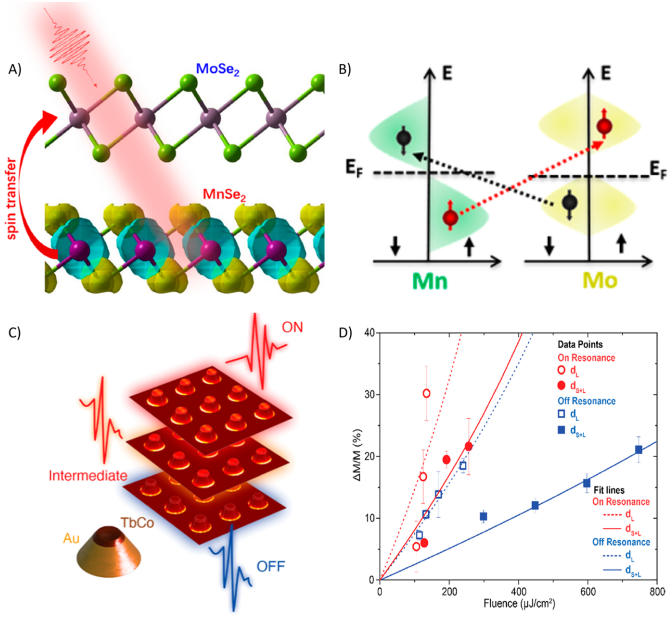


**Figure 12**
(A) Illustrates the atomic and electronic structure of $MoSe_2/MnSe_2$ vdW heterostructures. Side view of $MoSe_2/MnSe_2$ bilayers under photoexcitation, where purple, magenta and green represent Mo, Mn and Se atoms, respectively. (B) Density of states for Mn and Mo atoms on $MnSe_2$ and $MoSe_2$ layers, with red and black arrows denoting the pathway of photoexcited spin transfer from Mn to Mo atoms. (C) Regular array of truncated-nanocone-shaped Au–TbCo antennas. (D) Peak demagnetization values plotted against applied fluence. The solid data points correspond to measurements along a direction labeled $d_{S+L}$, while the open data points represent measurements along the perpendicular direction labeled $d_L$. Solid lines indicate Curie-law fits for data points along the $d_{S+L}$ direction, and dashed lines represent Curie-law fits for data points along the $d_L$ direction. Red data points and lines indicate on-resonance pumping, while blue data points and lines denote off-resonance pumping of the localized plasmon mode. Adapted with permission from He *et al.* (2022) (copyright 2022, American Chemical Society) and Mishra *et al.* (2022) (under a Creative Commons Attribution 4.0 International License, https://creativecommons.org/licenses/by/4.0/).

across a vdW-coupled interface [depicted in Figs. 12(A) and 12(B)], with a delay of approximately a few femtoseconds (He *et al.*, 2022). This delay proves to be highly contingent on laser duration and interlayer coupling, offering a means to modulate the amplitude and rate of spin transfer. Additionally, the study establishes that photoinduced ferromagnetic states can be achieved in other transition metal dichalcogenides, such as $PtS_2$ and $TaSe_2$ monolayers (Li, Zhou *et al.*, 2022). Overall, these findings offer a microscopic insight into optically controlled interlayer spin dynamics in 2D magnetic heterostructures, paving the way for manipulating magnetic order in 2D materials for ultrafast opto-spintronics. Moreover, Mishra *et al.* (2022) proposed a novel approach that not only facilitates light-driven bit downscaling but also reduces the required energy for magnetic memory writing while providing precise control over the degree of demagnetization in a magnetophotonic surface crystal. The system features a regular array of truncated-nanocone-shaped Au–TbCo antennas exhibiting both localized plasmon and surface lattice resonance modes [Fig. 12(C)]. The ultrafast magnetization dynamics of these nanoantennas reveal a threefold resonant enhancement in demagnetization efficiency. Additionally, the activation of surface lattice modes allows for the tuning of the degree of demagnetization [Fig. 12(D)]. This platform presents a unique opportunity where ultrafast demagnetization is localized at the nanoscale and can be controlled, offering a multistate system.

In summary, effective strategies for enhancing the Curie temperature of 2D magnets through chemical functionalization, isoelectronic substitution, alloying, strain engineering, defect engineering, electronic/magnetic field application, interlayer coupling, carrier doping, optical control and intercalation were recently reported (Jiang *et al.*, 2021). The ongoing research on 2D magnets with novel properties is anticipated to not only contribute to fundamental physics exploration but also advance the development of efficient, non-volatile memory, spin-based logic devices and spin-dependent optoelectronics. Additionally, understanding the interplay between magnetism and superconductivity, particularly in 2D superconductors, is crucial for high-temperature superconductivity and superconductor spintronics.

### 4.3. Catalysts

Catalytic reactions depend on thermodynamic energy barriers and kinetic processes, often facing trade-offs between reactant transport kinetics and local reaction kinetics. This dilemma can be addressed by engineering ordered structures that facilitate faster reactant transport and reduce the thermodynamic energy barrier of catalytic reactions (Mitchell *et al.*, 2021; Chen & Yu, 2020). As illustrated in Fig. 13(A), nanoscale-ordered catalytic Pt nanotubes, deposited periodically on a glassy carbon electrode, serve as active catalytic sites for methanol oxidation reactions (MOR) (Chen *et al.*, 2019). A comparison of methanol potential with ordered and disordered Pt nanotubes on the electrode surface reveals that ordered Pt nanotubes lead to lower methanol potential due to

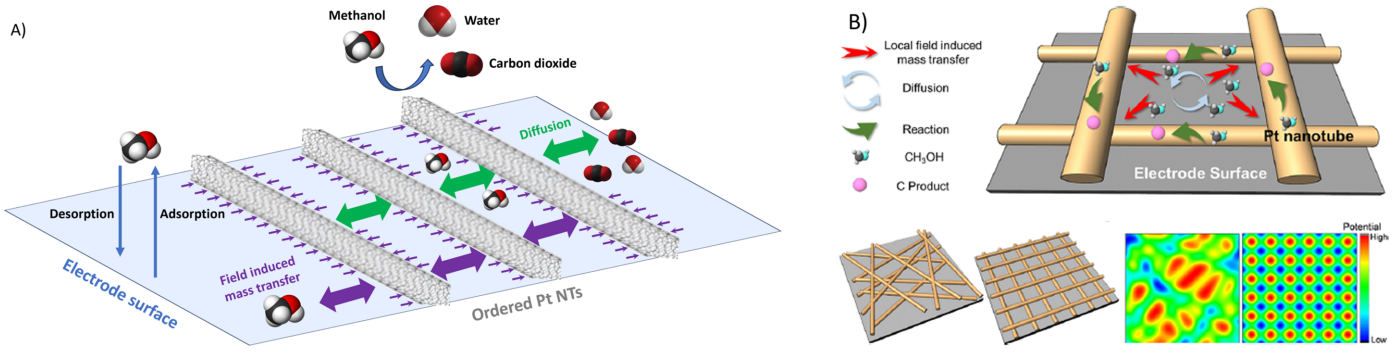


**Figure 13**
Structural ordering in catalytic materials. (A) Schematic of the kinetic model for MOR near ordered Pt nanotubes on an electrode surface. (B) Upper: a detailed kinetic model that encompasses the diffusion/local electric-field-induced mass transfer of MeOH and the surface reaction of MOR near the electrode surface. Bottom: illustration of 1D assemblies on the electrode surface and the interaction potentials of MeOH under the local electric field induced by both disordered and ordered configurations. Panel (B) reproduced with permission from Chen *et al.* (2021). Copyright 2021, American Chemical Society.

the existence of a microelectronic field. When Pt nanotubes are arranged periodically, methanol molecules are concentrated around the Pt catalytic sites, maximizing catalytic efficiency. In contrast, random and disordered Pt nanotubes result in an oversupply of methanol molecules at a single potential valley, reducing catalytic efficiency. Moreover, Chen *et al.* (2021) proposed a comprehensive kinetic model that couples mass transfer and surface reactions on the nanocatalyst-modified electrode surface [Fig. 13(B)]. This model aims to provide insights into and optimize the kinetics of electrocatalysis. Additionally, the authors demonstrate a theory-guided microchemical engineering (MCE) approach to systematically redesign catalysts for improved kinetics. Experimental investigations involving MOR reactions in a 3D-ordered channel with adjustable channel sizes validate the predictions made by calculations (Chen *et al.*, 2021). When employing the optimal channel size, both mass transfer and surface reactions in the channeled microreactor exhibit precise regulation. This MCE strategy represents a significant advancement in the design of structured catalysts and the modulation of kinetics (Chen *et al.*, 2021).

Achieving higher catalytic efficiency in the oxygen reduction reaction (ORR), a crucial process in fuel cell and metal–air battery electrodes, is of paramount importance while maintaining cleanliness and stability. Research has demonstrated that effective strategies involve heteroatom doping and structural optimization. In a recent study, Li, Fan *et al.* (2021) introduce a novel design featuring a single-atom-like B-$N_3$ configuration within ordered macroporous carbon (OMC) to catalyze the ORR efficiently, inspired by extensively studied transition metal $M$–$N_x$ sites. These B–$N_3$ structures are embedded in OMC (synthesized using a hydrogen-bonded organic framework as carbon and nitrogen sources), along with $SiO_2$ spheres as a template. The co-doping of B/N and the ordered macroporous structure significantly enhances the oxygen reduction catalytic performance in alkaline environments for this metal-free material (Li, Fan *et al.*, 2021). This research offers fresh insights into designing single-atom-like nonmetallic ORR electrocatalysts and fabricating ordered macroporous carbons based on hydrogen-bonded organic frameworks.

In addition, a comprehensive investigation to understand the impact on the band gaps of Ta–O–N functional materials of both composition variations ($\varepsilon$-$Ta_2O_5$, TaON and $Ta_3N_5$) and crystal structure variations ($\beta$-$Ta_2O_5$, $\delta$-$Ta_2O_5$, $\varepsilon$-$Ta_2O_5$ and amorphous $Ta_2O_5$) was conducted using DFT (Liu *et al.*, 2018). Findings indicate that the interactions between atomic core and valence electronic states, as well as the overlap between valence electronic states, significantly influence the band gap (Fig. 14). Considering their potential in photocatalytic water splitting and solar energy utilization, $Ta_3N_5$ and TaON are identified as promising materials for efficient photocatalysis, while $\delta$-$Ta_2O_5$ is suited for photocatalytic degradation of various pollutants due to its oxidation potential and suitable band gap for visible light absorption. Although amorphous $Ta_2O_5$, $\varepsilon$-$Ta_2O_5$ and $\beta$-$Ta_2O_5$ are not ideal for direct use as photocatalysts, they can serve as modifiers for conventional Ta–O–N photocatalysts, given their similar

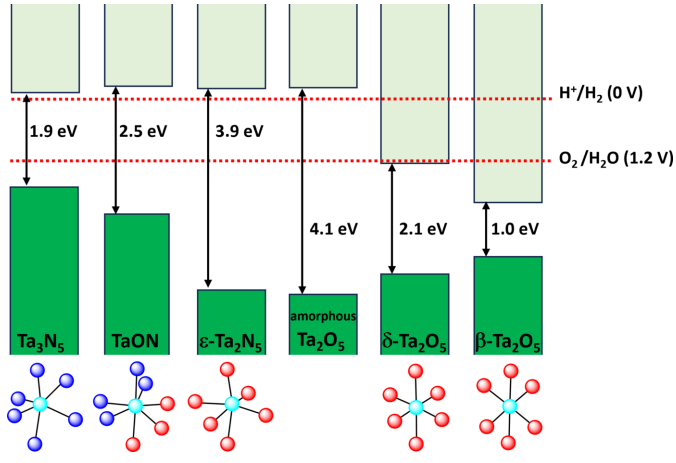


**Figure 14**
Diagram of polyhedrons and calculated positions of the valence and conduction band edges of different Ta–O–N materials (vacuum level, in eV) and the potential in V (versus NHE). The two dashed horizontal red lines represent the redox potentials of water.

composition and structure. These results offer valuable reference data for analyzing the optical properties of more intricate Ta–O–N functional materials and provide insights for designing novel Ta–O–N materials tailored to specific optoelectronic applications by adjusting composition and crystal structure.

Catalytic processes depend on the interactions between materials and reactants at the atomic level. Synchrotron radiation and XFELs equipped for advanced techniques, such as X-ray emission spectroscopy (XES) (Alonso-Mori *et al.*, 2020) and X-ray absorption spectroscopy (XAS) (Diesen *et al.*, 2021) allow one to probe the electronic structures of materials, offering a better understanding of the mechanisms behind catalytic reactions (Bergmann *et al.*, 2021; Cao *et al.*, 2023). Moreover, Bragg geometry coherent X-ray diffraction imaging (BCDI) permits obtaining the shape of an object as well as the displacements and strains (Robinson & Harder, 2009). Finally, time-resolved BCDI measurements with XFELs provide kinetic information of the internal displacement distribution, with ≥100 times higher time resolution than synchrotron sources due to their intense and fully transversely coherent X-ray beam (Bergmann *et al.*, 2021; Cao *et al.*, 2023).

Zeolites are three-dimensional aluminosilicates with unique properties attributed to the characteristics of their sub-nanometre pores, the Si/Al ratio in the framework and the charge-balancing cations. In addition, the range of atoms used in framework building has expanded beyond the original Si and Al to include Sn, P, Ti, Fe and Zr, among others. Currently, natural or synthetic zeolites have over 250 distinct framework types identified (Baerlocher *et al.*, 2023). The non-uniform distribution of these cations significantly impacts catalytic performance by affecting the diffusion rates of reactants and products within the crystal (Xu & Wu, 2022). Zeolites are widely researched for their efficient catalytic properties due to their well defined pores and high chemical, thermal and mechanical stabilities (Li *et al.*, 2017; Hullfish *et al.*, 2023). The catalytic applications of zeolite materials have expanded beyond conventional single functionalities, such as solid acids or selective oxidation catalysts, to bi/multifunctionalities through combination with metals or metal oxides (Xu & Wu, 2022). Zeolites are an excellent example in catalytic science of the crucial role of structure in function. The pore structure can control selectivity, making it a key factor in determining the effectiveness of the catalyst. To adjust the pore structure of zeolites, it is possible to alter the composition and bulk framework. Moreover, to enhance selective adsorption, the external surface of zeolites can be modified with an additional diffusion layer or functional group (Peng *et al.*, 2020). Another approach is to adjust the pore openings of zeolites to improve adsorption selectivity (Zhou *et al.*, 2022).

Nevertheless, conventional analytical tools do not capture structural deformations associated with non-uniform active regions during catalysis. In a recent study *in situ* XFEL-based time-resolved coherent X-ray diffraction imaging was employed to investigate the internal deformations arising from the non-uniform distribution of Cu ions in Cu-exchanged ZSM-5 zeolite ($Na_nAl_nSi_{96-n}O_{192}\cdot 16H_2O$, $0 < n < 27$) crystals during the deoxygenation of nitrogen oxides with propene (see Fig. 15) (Kang *et al.*, 2020). Findings reveal that interactions between reactants and active sites result in an unusual strain distribution. These insights shed light on the significance of structural non-uniformity in zeolites during catalysis and will aid in the future design of zeolites for various applications.

Finally, metal centers in metalloenzymes and molecular catalysts play a crucial role in facilitating complex chemical reactions by orchestrating the rearrangement of atoms and electrons, controlling charge and spin transfer, and influencing bond formation and cleavage. A prominent illustration of simultaneous XES and XRD applications can be found in the extensive studies on photosystem II (PSII) crystals (Ibrahim *et al.*, 2020). PSII, a metalloenzyme, drives the light-induced four-step oxidation of water to produce molecular oxygen (as shown in Fig. 16) and has been extensively investigated using XFELs (Ibrahim *et al.*, 2020). XFELs, with their ultrafast pulses, can effectively mitigate radiation damage. Within the PSII catalytic site lies a $Mn_4CaO_5$ cluster embedded in a large protein complex, and each step of the reaction cycle is initiated by photon absorption. The $Mn_4CaO_5$ cluster accumulates charges, eventually catalyzing the oxidation of two water molecules, which results in the release of molecular oxygen,

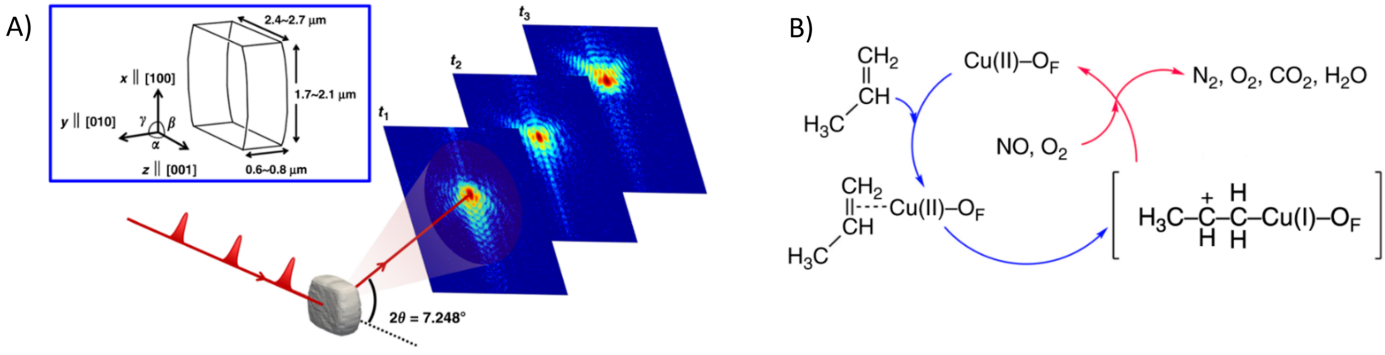


**Figure 15**
Experimental principles and reactions. (A) Scheme of the *in situ* XFEL-based time-resolved coherent X-ray diffraction imaging experiment. The Cu–ZSM-5 is a monoclinic structure, where $\alpha \cong 90.4°$ and $\beta = \gamma = 90°$. (B) Catalytic deoxygenation reactions in the Cu–ZSM-5. Propene adsorption (in blue) and $NO_x$ deoxygenation (in red) by inserting NO and $O_2$ in the presence of adsorbed propene molecules. Reproduced from Kang *et al.* (2020) under a Creative Commons Attribution 4.0 International License, https://creativecommons.org/licenses/by/4.0/.

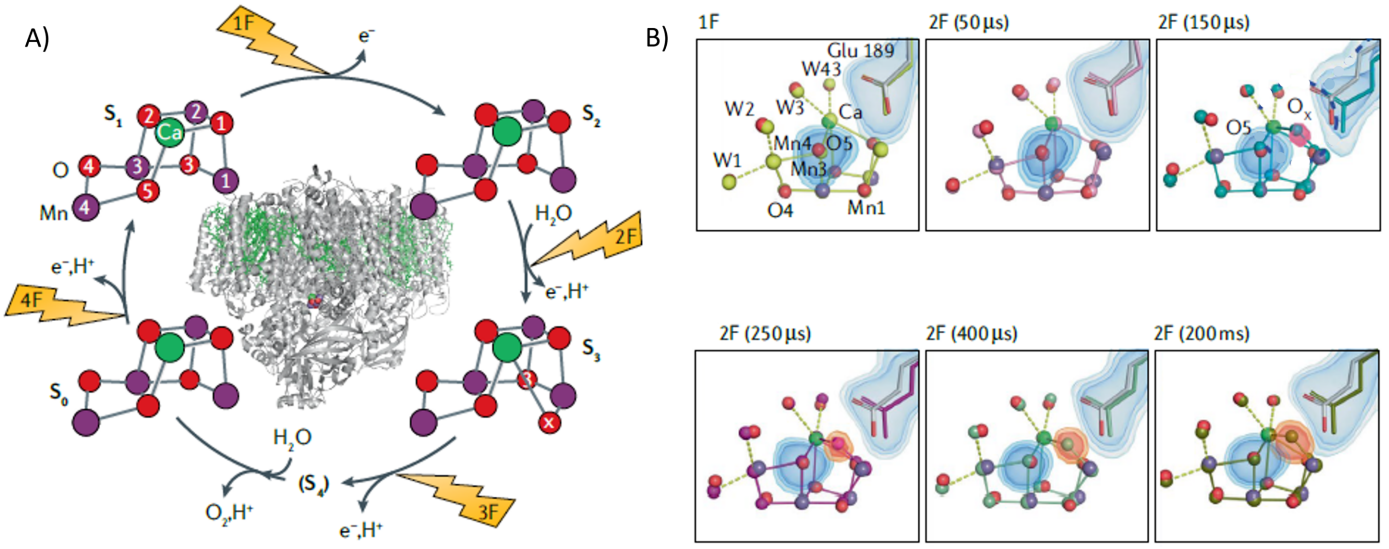


**Figure 16**
Combined XRD and XES structural studies on photosystem II. (A) The overall structure of the protein and the four-step catalytic cycle (Kok cycle), revealed by flashes 1F–4F. For each of the stable states S0, S1, S2 and S3, the XRD structures of the catalytic $Mn_4Ca$ clusters (O in red, Mn in pruple and Ca in green) obtained from X-ray free-electron laser measurements are also shown. (B) Results from time-resolved XES and XRD measurements, together with kinetic simulations based on previous infrared (IR) or XAS measurements. Adapted from Ibrahim *et al.* (2020) under a Creative Commons Attribution NonCommercial-NoDerivs 4.0 International License, https://creativecommons.org/licenses/by/4.0/.

four protons and four electrons. Combined XRD and XES analyses initially confirmed that the $Mn_4CaO_5$ cluster in PSII microcrystals used for diffraction measurements remained in an intact non-reduced state. Simultaneously acquired XES–XRD data revealed that the Mn cluster undergoes a structural rearrangement during the S2 to S3 transition (Ibrahim *et al.*, 2020). This rearrangement includes cluster widening and the insertion of an additional oxygen bridge between Mn and Ca, forming a $Mn_4CaO_6$ cluster. Subsequent time-resolved data collection using XES and XRD unveiled that this transition occurs with a time constant of approximately 300 µs. Moreover, the structural data indicated that certain amino acid residues in the vicinity of the $Mn_4CaO_5$ cluster experience structural changes before the metal cluster expands and the new oxygen bridge is inserted. The simultaneous XES and XRD approach facilitated the conclusion that Mn oxidation and oxygen insertion occur simultaneously during this transition.

## 5. In conclusion

Structural sciences stand as indispensable contributors to the advancement of functional materials, offering a holistic insight into atomic and molecular arrangements, crystal structures, chemical compositions, defect characteristics, and material dynamics. This profound understanding empowers researchers to craft of materials with tailored functionalities, thereby fueling innovation across diverse sectors such as electronics, energy storage, catalysis and beyond. The continuous progression of these sciences is poised to play a pivotal role in shaping the materials of the future and their transformative impact on technology and society. The IUCr, through its ongoing commitment to research and global scientific collaboration, plays a crucial role in driving the development of new functional materials by providing an international platform that facilitates the exchange of knowledge, promotes innovative discoveries, and fosters networking among scientists and crystallographers worldwide.

Over the past decade, a convergence of cutting-edge technologies, including X-ray free-electron lasers, electron diffraction techniques and computational methods, has sparked a revolution in the characterization of materials. These groundbreaking tools have significantly enhanced our comprehension of functional materials, enabling in-depth explorations into atomic structures, dynamic processes, electronic properties, phase transitions and the behavior of materials under extreme conditions. Particularly, XFELs have pushed the boundaries of materials science, facilitating exploration at the atomic and molecular levels and driving innovations across various technological domains. In the broader landscape of materials science, precession electron diffraction tomography has emerged as a transformative technique, expediting the discovery and design of novel functional materials. The capacity of PEDT to offer a comprehensive three-dimensional view of crystal structure, coupled with its ability to capture dynamic processes, positions it as an indispensable tool for researchers at the forefront of materials innovation. Simultaneously, computational methods have risen as a cost-effective, efficient and complementary approach to materials research, further hastening the development of innovative materials for a broad spectrum of applications.

As these technologies progress, I envision the emergence of even more revolutionary discoveries and applications in the domain of functional materials, solidifying the pivotal role of these scientific advancements in shaping our future.

Unraveling the intricacies of complex materials' functions hinges on understanding their atomic-scale structures and their dynamic process, representing a critical challenge. Thus, the current imperative is to devise and implement a consistent methodology capable of seamlessly integrating diverse yet complementary measurements within the field of structural sciences. The narrative of functional materials stands as a testament to human ingenuity, curiosity and an enduring commitment to progress. From the early days of fire and metalworking to the forefront of modern nanotechnology, these materials have consistently reshaped societies and will undoubtedly continue to do so in the future.

## Acknowledgements

The author extends his gratitude to all the contributing authors who enriched this work with their insights. Special thanks are also due to the co-chair of the microsymposium, Dr Dmitry Golberg. Significantly, this congress marked the 75th anniversary of the IUCr, adding a special dimension to the event (Allen, 2023). SAS is a member of the research staff of CONICET and a Professor at the University of Buenos Aires.

## Funding information

The following funding is acknowledged: Universidad de Buenos Aires (grant No. 20020190200010BA); Consejo Nacional de Investigaciones Científicas y Técnicas (grant No. 28720210100267CO); Agencia Nacional de Promoción de la Investigación, el Desarrollo Tecnológico y la Innovación (grant No. PICT-2019-2019-00123).

## References

Abakumov, A. M., Fedotov, S. S., Antipov, E. V. & Tarascon, J.-M. (2020). *Nat. Commun.* **11**, 4976.
Abd Mutalib, M., Rahman, M. A., Othman, M. H. D., Ismail, A. F. & Jaafar, J. (2017). *Membrane Characterization*, edited by N. Hilal, A. F. Ismail, T. Matsuura & D. Oatley-Radcliffe, pp. 161–179. Amsterdam: Elsevier.
Ai, J., Zhang, X., Bai, T., Shen, Q., Oleynikov, P., Duan, Y., Terasaki, O., Che, S. & Han, L. (2022). *Nat. Commun.* **13**, 5718.
Aizenberg, J. & Levkin, P. A. (2020). *Adv. Funct. Mater.* **30**, 2002785.
Akkuratov, V., Blagov, A., Eliovich, Y., Targonskii, A., Pisarevsky, Y., Protsenko, A., Shishkov, V. & Kovalchuk, M. (2022). *J. Appl. Cryst.* **55**, 80–89.
Akl, A. A. & Hassanien, A. S. (2021). *Physica B*, **620**, 413267.
Allen, A. (2023). *IUCrJ*, **10**, 509–518.
Alonso-Mori, R., Sokaras, D., Cammarata, M., Ding, Y., Feng, Y., Fritz, D., Gaffney, K. J., Hastings, J., Kao, C.-C., Lemke, H. T., Maxwell, T., Robert, A., Schropp, A., Seiboth, F., Sikorski, M., Song, S., Weng, T.-C., Zhang, W., Glenzer, S., Bergmann, U. & Zhu, D. (2020). *Sci. Rep.* **10**, 16837.
Asakura, K., Gaffney, K. J., Milne, C. & Yabashi, M. (2020). *Phys. Chem. Chem. Phys.* **22**, 2612–2614.
Asrafusjaman, M., Islam, J., Rahman, M. A. & Hossain, A. K. M. A. (2023). *ACS Omega*, **8**, 21813–21822.
Atinafu, D. G., Yun, B. Y., Kim, Y. U. & Kim, S. (2023). *Small Methods*, **7**, 2201515.
Azamal Husen, K. S. S. (2023). *Advances in Smart Nanomaterials and Their Applications*. Cambridge: Elsevier.
Baerlocher, Ch., Brouwer, D., Marler, B. & McCusker, L. B. (2023). *Database of Zeolite Structures*, https://www.iza-structure.org/databases/.
Baird, S. G., Diep, T. Q. & Sparks, T. D. (2022). *Digit. Discov.* **1**, 226–240.
Bandyopadhyay, A., Bacaksiz, C., He, J. & Frauenheim, T. (2021). *J. Phys. Chem. Lett.* **12**, 11308–11315.
Bandyopadhyay, A., Li, S. & Frauenheim, T. (2022). *J. Phys. Chem. Lett.* **13**, 6755–6761.
Batuk, M., Vandemeulebroucke, D., Ceretti, M., Paulus, W. & Hadermann, J. (2023). *J. Mater. Chem. A*, **11**, 213–220.
Bergmann, U., Kern, J., Schoenlein, R. W., Wernet, P., Yachandra, V. K. & Yano, J. (2021). *Nat. Rev. Phys.* **3**, 264–282.
Bhaskar, G., Gvozdetskyi, V., Batuk, M., Wiaderek, K. M., Sun, Y., Wang, R., Zhang, C., Carnahan, S. L., Wu, X., Ribeiro, R. A., Bud'ko, S. L., Canfield, P. C., Huang, W., Rossini, A. J., Wang, C.-Z., Ho, K.-M., Hadermann, J. & Zaikina, J. V. (2021). *J. Am. Chem. Soc.* **143**, 4213–4223.
Boothroyd, A. T. (2020). *Principles of Neutron Scattering from Condensed Matter*. Oxford University Press.
Borgmans, S., Rogge, S. M. J., De Vos, J. S., Stevens, C. V., Van Der Voort, P. & Van Speybroeck, V. (2021). *Angew. Chem. Int. Ed.* **60**, 8913–8922.
Boullay, P., Palatinus, L. & Barrier, N. (2013). *Inorg. Chem.* **52**, 6127–6135.
Bourgeois, L., Zhang, Y., Zhang, Z., Chen, Y. & Medhekar, N. V. (2020). *Nat. Commun.* **11**, 1248.
Broadhurst, E. T., Xu, H., Clabbers, M. T. B., Lightowler, M., Nudelman, F., Zou, X. & Parsons, S. (2020). *IUCrJ*, **7**, 5–9.
Bunker, G. (2010). *Introduction to XAFS*. Cambridge University Press.
Cao, D., Xu, W., Chen, S., Liu, C., Sheng, B., Song, P., Moses, O. A., Song, L. & Wei, S. (2023). *Adv. Mater.* **35**, 2205346.
Catlow, C. R. A. (2018). *IUCrJ*, **5**, 1–3.
Chen, B., Shen, Y., Chen, Q. & Chen, L. (2022). *Curr. Opin. Green Sustain. Chem.* **37**, 100658.
Chen, J., Xiao, J., Li, J., Gao, H., Guo, X., Liu, H. & Wang, G. (2022). *J. Mater. Chem. A*, **10**, 20635–20645.
Chen, Q.-X., Liu, Y.-H., He, Z., Wang, J.-L., Liu, J.-W., Jiang, H.-J., Huang, W.-R., Gao, G.-Y., Hou, Z.-H. & Yu, S.-H. (2021). *J. Am. Chem. Soc.* **143**, 12600–12608.
Chen, Q.-X., Liu, Y.-H., Qi, X.-Z., Liu, J.-W., Jiang, H.-J., Wang, J.-L., He, Z., Ren, X.-F., Hou, Z.-H. & Yu, S.-H. (2019). *J. Am. Chem. Soc.* **141**, 10729–10735.
Chen, Q.-X. & Yu, S.-H. (2020). *Trends Chem.* **2**, 888–897.
Cheng, X., Li, Y., Cao, T., Wu, R., Wang, M., Liu, H., Liu, X., Lu, J. & Zhang, Y. (2021). *ACS Energy Lett.* **6**, 1703–1710.
Cheng, Z., Wang, C., Wu, X. & Chu, J. (2022). *J. Semicond.* **43**, 081001.
Choi, E. H., Lee, Y., Heo, J. & Ihee, H. (2022). *Chem. Sci.* **13**, 8457–8490.
Cruz-Cabeza, A. J. (2016). *Acta Cryst.* B**72**, 437–438.
Dada, M., Popoola, P. & Mathe, N. (2023). *World J. Eng.* **20**, 43–74.
Das, P., Chakraborty, G., Tyagi, S. & Mandal, S. K. (2020). *Appl. Mater. Interfaces*, **12**, 52527–52537.
Day, A. C., Breen, A. J., Reinhard, D. A., Kelly, T. F. & Ringer, S. P. (2022). *Ultramicroscopy*, **241**, 113595.
Diesen, E., Wang, H.-Y., Schreck, S., Weston, M., Ogasawara, H., LaRue, J., Perakis, F., Dell'Angela, M., Capotondi, F., Giannessi, L., Pedersoli, E., Naumenko, D., Nikolov, I., Raimondi, L., Spezzani, C., Beye, M., Cavalca, F., Liu, B., Gladh, J., Koroidov, S., Miedema, P. S., Costantini, R., Heinz, T. F., Abild-Pedersen, F., Voss, J., Luntz, A. C. & Nilsson, A. (2021). *Phys. Rev. Lett.* **127**, 016802.
Faustini, M., Nicole, L., Ruiz–Hitzky, E. & Sanchez, C. (2018). *Adv. Funct. Mater.* **28**, 1704158.
Firestein, K. L., von Treifeldt, J. E., Kvashnin, D. G., Fernando, J. F. S., Zhang, C., Kvashnin, A. G., Podryabinkin, E. V., Shapeev, A. V., Siriwardena, D. P., Sorokin, P. B. & Golberg, D. (2020). *Nano Lett.* **20**, 5900–5908.

Freund, R., Lanza, A. E., Canossa, S., Gemmi, M., Goscianska, J., Cauda, V., Oschatz, M. & Wuttke, S. (2023). *Chem. Mater.* **35**, 1891–1900.
Frolov, A. S., Sánchez-Barriga, J., Callaert, C., Hadermann, J., Fedorov, A. V., Usachov, D. Yu., Chaika, A. N., Walls, B. C., Zhussupbekov, K., Shvets, I. V., Muntwiler, M., Amati, M., Gregoratti, L., Varykhalov, A. Yu., Rader, O. & Yashina, L. V. (2020). *ACS Nano*, **14**, 16576–16589.
Gao, Z., Li, A., Ma, D. & Zhou, W. (2022). *Top. Catal.* **65**, 1609–1619.
Gemmi, M., Mugnaioli, E., Gorelik, T. E., Kolb, U., Palatinus, L., Boullay, P., Hovmöller, S. & Abrahams, J. P. (2019). *ACS Cent. Sci.* **5**, 1315–1329.
Goonetilleke, D. & Sharma, N. (2021). *Phys. Sci. Rev.* **6**, 20180155.
Grigoriev, S. A. (2021). *Geoarchaeology and Archaeological Mineralogy. GAM 2019*. Springer Proceedings in Earth and Environmental Sciences, pp. 83–89. https://doi.org/10.1007/978-3-030-48864-2_12. Cham: Springer.
Gruene, T., Holstein, J. J., Clever, G. H. & Keppler, B. (2021). *Nat. Rev. Chem.* **5**, 660–668.
Han, Y., Das, P., He, Y., Sorescu, D. C., Jordan, K. D. & Rosi, N. L. (2022). *J. Am. Chem. Soc.* **144**, 19567–19575.
Hansen, T. C. & Kohlmann, H. (2014). *Z. Anorg. Allg. Chem.* **640**, 3044–3063.
He, J., Li, S., Zhou, L. & Frauenheim, T. (2022). *J. Phys. Chem. Lett.* **13**, 2765–2771.
Hehn, A.-S., Sertcan, B., Belleflamme, F., Chulkov, S. K., Watkins, M. B. & Hutter, J. (2022). *J. Chem. Theory Comput.* **18**, 4186–4202.
Heilbron, J. L. (2022). *Electricity in the 17th and 18th Centuries: a Study of Early Modern Physics*. Berkeley: University of California Press.
Holstad, T. S., Dresselhaus-Marais, L. E., Raeder, T. M., Kozioziemski, B., Driel, T., Seaberg, M., Folsom, E., Eggert, J. H., Knudsen, E. B., Nielsen, M. M., Simons, H., Haldrup, K. & Poulsen, H. F. (2023). *Proc. Natl Acad. Sci. USA*, **120**, e2307049120.
Hsu, Y., Yang, Z. & Buehler, M. J. (2022). *APL Mater.* **10**, 041107.
Huang, N., Deng, H., Liu, B., Wang, D. & Zhao, Z. (2021). *Innovation*, **2**, 100097.
Hullfish, C. W., Tan, J. Z., Adawi, H. I. & Sarazen, M. L. (2023). *ACS Catal.* **13**, 13140–13150.
Hummel, R. E. (2004). *Understanding Materials Science*. New York: Springer.
Hyun, G., Cao, S., Ham, Y., Youn, D.-Y., Kim, I.-D., Chen, X. & Jeon, S. (2022). *ACS Nano*, **16**, 9762–9771.
Ibrahim, M., Fransson, T., Chatterjee, R., Cheah, M. H., Hussein, R., Lassalle, L., Sutherlin, K. D., Young, I. D., Fuller, F. D., Gul, S., Kim, I.-S., Simon, P. S., de Lichtenberg, C., Chernev, P., Bogacz, I., Pham, C. C., Orville, A. M., Saichek, N., Northen, T., Batyuk, A., Carbajo, S., Alonso-Mori, R., Tono, K., Owada, S., Bhowmick, A., Bolotovsky, R., Mendez, D., Moriarty, N. W., Holton, J. M., Dobbek, H., Brewster, A. S., Adams, P. D., Sauter, N. K., Bergmann, U., Zouni, A., Messinger, J., Kern, J., Yachandra, V. K. & Yano, J. (2020). *Proc. Natl Acad. Sci. USA*, **117**, 12624–12635.
Islam, J. & Hossain, A. K. M. A. (2020). *Sci. Rep.* **10**, 14391.
Isnard, O. (2007). *C. R. Phys.* **8**, 789–805.
Jaeschke, E. J., Khan, S., Schneider, J. R. & Hastings, J. B. (2020). *Synchrotron Light Sources and Free-Electron Lasers*. Cham: Springer International Publishing.
Jia, Q., Zhang, F., Rometsch, P., Li, J., Mata, J., Weyland, M., Bourgeois, L., Sui, M. & Wu, X. (2020). *Acta Mater.* **193**, 239–251.
Jiang, X., Liu, Q., Xing, J., Liu, N., Guo, Y., Liu, Z. & Zhao, J. (2021). *Appl. Phys. Rev.* **8**, 031305.
Joseph, A. (2020). *Micro and Nanostructured Composite Materials for Neutron Shielding Applications*, pp. 355–378. Oxford: Elsevier.
Ju, Z., Xu, X., Zhang, X., Raigama, K. U. & Yu, G. (2023). *Chem. Eng. J.* **454**, 140003.
Kalhor, P., Jung, N., Bräse, S., Wöll, C., Tsotsalas, M. & Friederich, P. (2024). *Adv. Funct. Mater.* **34**, 2302630.
Kang, J., Carnis, J., Kim, D., Chung, M., Kim, J., Yun, K., An, G., Cha, W., Harder, R., Song, S., Sikorski, M., Robert, A., Thanh, N. H., Lee, H., Choi, Y. N., Huang, X., Chu, Y. S., Clark, J. N., Song, M. K., Yoon, K. B., Robinson, I. K. & Kim, H. (2020). *Nat. Commun.* **11**, 5901.
Karakulina, O. M., Demortière, A., Dachraoui, W., Abakumov, A. M. & Hadermann, J. (2018). *Nano Lett.* **18**, 6286–6291.
Klar, P. B., Krysiak, Y., Xu, H., Steciuk, G., Cho, J., Zou, X. & Palatinus, L. (2023). *Nat. Chem.* **15**, 848–855.
Ko, W., Ma, C., Nguyen, G. D., Kolmer, M. & Li, A. (2019). *Adv. Funct. Mater.* **29**, 1903770.
Kolb, U., Gorelik, T., Kübel, C., Otten, M. T. & Hubert, D. (2007). *Ultramicroscopy*, **107**, 507–513.
Krishna, D. N. G. & Philip, J. (2022). *Appl. Surf. Sci. Adv.* **12**, 100332.
Li, D., Li, S., Zhong, C. & He, J. (2021). *Nanoscale*, **13**, 19812–19827.
Li, G., Zhang, H. & Han, Y. (2023). *Chem. Rev.* **123**, 10728–10749.
Li, J., Cai, J., Yu, J., Li, Z. & Ding, B. (2023). *Adv. Funct. Mater.* **33**, 2303249.
Li, J., Sharma, N., Jiang, Z., Yang, Y., Monaco, F., Xu, Z., Hou, D., Ratner, D., Pianetta, P., Cloetens, P., Lin, F., Zhao, K. & Liu, Y. (2022). *Science*, **376**, 517–521.
Li, S., Zhou, L., Frauenheim, T. & He, J. (2022). *J. Phys. Chem. Lett.* **13**, 6223–6229.
Li, W., Zhu, W., Zhang, G., Wu, H., Zhu, S., Li, R., Zhang, E., Zhang, X., Deng, Y., Zhang, J., Zhao, L., Chang, H. & Wang, K. (2023). *Adv. Mater.* **35**, 2303688.
Li, X., Fan, L., Xu, B., Shang, Y., Li, M., Zhang, L., Liu, S., Kang, Z., Liu, Z., Lu, X. & Sun, D. (2021). *Appl. Mater. Interfaces*, **13**, 53892–53903.
Li, X., Lou, L., Li, Y., Zhang, G., Hua, Y., Li, W., Zhang, H.-T., Yue, M. & Zhang, X. (2022). *Nano Lett.* **22**, 7644–7650.
Li, Y., Li, L. & Yu, J. (2017). *Chem*, **3**, 928–949.
Li, Z., Yang, J., Zhou, Z., Mao, C., Li, Z., Li, G. & Zhang, Z. (2023). *Appl. Surf. Sci.* **621**, 156785.
Liebschner, D., Afonine, P. V., Baker, M. L., Bunkóczi, G., Chen, V. B., Croll, T. I., Hintze, B., Hung, L.-W., Jain, S., McCoy, A. J., Moriarty, N. W., Oeffner, R. D., Poon, B. K., Prisant, M. G., Read, R. J., Richardson, J. S., Richardson, D. C., Sammito, M. D., Sobolev, O. V., Stockwell, D. H., Terwilliger, T. C., Urzhumtsev, A. G., Videau, L. L., Williams, C. J. & Adams, P. D. (2019). *Acta Cryst.* D**75**, 861–877.
Lim, H., Kim, H. S., Qazi, R., Kwon, Y., Jeong, J. & Yeo, W. (2020). *Adv. Mater.* **32**, 1901924.
Lin, F., Zhao, K. & Liu, Y. (2021). *ACS Energy Lett.* **6**, 4065–4070.
Liu, H., Nomoto, K., Ceguerra, A. V., Kruzic, J. J., Cairney, J. & Ringer, S. P. (2023). *J. Appl. Cryst.* **56**, 889–902.
Liu, L., Jiang, J.-T., Cui, X.-Y., Zhang, B., Zhen, L. & Ringer, S. P. (2022). *J. Mater. Sci. Technol.* **99**, 61–72.
Liu, Q.-L., Zhao, Z.-Y. & Yi, J.-H. (2018). *Phys. Chem. Chem. Phys.* **20**, 12005–12015.
Lou, L., Li, Y., Li, X., Li, H., Li, W., Hua, Y., Xia, W., Zhao, Z., Zhang, H., Yue, M. & Zhang, X. (2021). *Adv. Mater.* **33**, 2102800.
Lv, H., da Silva, A., Figueroa, A. I., Guillemard, C., Aguirre, I. F., Camosi, L., Aballe, L., Valvidares, M., Valenzuela, S. O., Schubert, J., Schmidbauer, M., Herfort, J., Hanke, M., Trampert, A., Engel-Herbert, R., Ramsteiner, M. & Lopes, J. M. J. (2023). *Small*, **19**, 2302387.
Merchant, A., Batzner, S., Schoenholz, S. S., Aykol, M., Cheon, G. & Cubuk, E. D. (2023). *Nature*, **624**, 80–85.
Mishra, K., Rowan-Robinson, R. M., Ciuciulkaite, A., Davies, C. S., Dmitriev, A., Kapaklis, V., Kimel, A. V. & Kirilyuk, A. (2022). *Nano Lett.* **22**, 9773–9780.
Mitchell, S., Qin, R., Zheng, N. & Pérez-Ramírez, J. (2021). *Nat. Nanotechnol.* **16**, 129–139.
Murrie, R. P., Werdiger, F., Donnelley, M., Lin, Y., Carnibella, R. P., Samarage, C. R., Pinar, I., Preissner, M., Wang, J., Li, J., Morgan, K. S., Parsons, D. W., Dubsky, S. & Fouras, A. (2020). *Sci. Rep.* **10**, 447.
Neu, J. (2023). *APL Photon.* **8**, 071103.

Neverov, V. D., Lukyanov, A. E., Krasavin, A. V., Vagov, A. & Croitoru, M. D. (2022). *Commun. Phys.* **5**, 177.
Norton, M. G. (2021). *Ten Materials That Shaped Our World*, pp. 7–23. Cham: Springer International Publishing.
Palatinus, L., Brázda, P., Jelínek, M., Hrdá, J., Steciuk, G. & Klementová, M. (2019). *Acta Cryst.* B**75**, 512–522.
Pandey, R., Wang, N., Sahu, B. B., Moharana, S. & Tiwari, S. K. (2023). *Nanoparticles Reinforced Metal Nanocomposites*, pp. 1–21. Singapore: Springer Nature.
Peng, P., Stosic, D., Liu, X.-M., Yan, Z.-F. & Mintova, S. (2020). *Chem. Eng. J.* **385**, 123800.
Prescott, G. B. (2022). *History, Theory, and Practice of the Electric Telegraph*. BoD–Books on Demand.
Preuss, K., Howarth, A. & Dawe, L. (2020). *Cryst. Growth Des.* **20**, 7565–7567.
Qiu, X., Wang, X., He, Y., Liang, J., Liang, K., Tardy, B. L., Richardson, J. J., Hu, M., Wu, H., Zhang, Y., Rojas, O. J., Manners, I. & Guo, J. (2021). *Sci. Adv.* **7**, eabh3482.
Rauch, E. F., Véron, M., Portillo, J., Bultreys, D., Maniette, Y. & Nicolopoulos, S. (2008). *Microsc. Anal.* **22**, S5–S8.
Richet, P. (2021). *Encyclopedia of Glass Science, Technology, History, and Culture*, Vol. 2, pp. 1387–1412. Hoboken: Wiley.
Ridley, C. J. & Kamenev, K. V. (2014). *Z. Kristallogr. Cryst. Mater.* **229**, 171–179
Robinson, I. & Harder, R. (2009). *Nat. Mater.* **8**, 291–298.
Saha, A., Nia, S. S. & Rodríguez, J. A. (2022). *Chem. Rev.* **122**, 13883–13914.
Sanderson, K. & Castelvecchi, D. (2023). *Nature*, **622**, 227–228.
Santos, D. A., Rezaei, S., Zhang, D., Luo, Y., Lin, B., Balakrishna, A. R., Xu, B.-X. & Banerjee, S. (2023). *Chem. Sci.* **14**, 458–484.
Shahed, H., Sharma, N., Angst, M., Voigt, J., Perßon, J., Prakash, P., Törnroos, K. W., Chernyshov, D., Gildenast, H., Ohl, M., Saffarini, G., Grzechnik, A. & Friese, K. (2023). *Acta Cryst.* B**79**, 354–367.
Smieska, L., Page, K. A., Ree, B., Zheng, B., Koerner, H. & Woll, A. R. (2023). *Synchrotron Radiat. News*. **36**(2), 4–11.
Špelda, D. (2019). *Seventeenth Century*, **34**, 107–126.
Spies, J. A., Neu, J., Tayvah, U. T., Capobianco, M. D., Pattengale, B., Ostresh, S. & Schmuttenmaer, C. A. (2020). *J. Phys. Chem. C*, **124**, 22335–22346.
Sun, F., Wang, C., Osenberg, M., Dong, K., Zhang, S., Yang, C., Wang, Y., Hilger, A., Zhang, J., Dong, S., Markötter, H., Manke, I. & Cui, G. (2022). *Adv. Energy Mater.* **12**, 2103714.
Szydło, Z. A. (2022). *Pure Appl. Chem.* **94**, 869–888.
Taylor, R. & Wood, P. A. (2019). *Chem. Rev.* **119**, 9427–9477.
Todorović, M., Gutmann, M. U., Corander, J. & Rinke, P. (2019). *NPJ Comput Mater* **5**, 35.
Tsuji, K., Matsuno, T., Takimoto, Y., Yamanashi, M., Kometani, N., Sasaki, Y. C., Hasegawa, T., Kato, S., Yamada, T., Shoji, T. & Kawahara, N. (2015). *At. Spectrosc.* **113**, 43–53.
Wan, X., Li, Z., Yu, W., Wang, A., Ke, X., Guo, H., Su, J., Li, L., Gui, Q., Zhao, S., Robertson, J., Zhang, Z. & Guo, Y. (2023). *Adv. Mater.* 2305192.
Wang, C. & Sun, C. C. (2019). *Mol. Pharm.* **16**, 1732–1741.
Wang, L., Li, Z., Wu, Q., Huang, Z., Yuan, L., Chai, Z. & Shi, W. (2020). *Environ. Sci. Nano*, **7**, 724–752.
Wang, X., Huang, S.-C., Hu, S., Yan, S. & Ren, B. (2020). *Nat. Rev. Phys.* **2**, 253–271.
Wei, Y., Yang, C., Jiang, H., Li, Q., Che, F., Wan, S., Yao, S., Gao, F., Zhang, T., Wang, J. & Song, B. (2022). *Insights Imaging*, **13**, 135.
Willmott, P. (2011). *An Introduction to Synchrotron Radiation*. Chichester: Wiley.
Woodley, S. M., Day, G. M. & Catlow, R. (2020). *Philos. Trans. R. Soc. A*, **378**, 20190600.
Wu, S., Li, J., Ling, Y., Sun, T., Fan, Y., Yu, J., Terasaki, O. & Ma, Y. (2022). *Chem. Mater.* **34**, 8119–8126.
Xiang, C., Han, E.-H., Zhang, Z. M., Fu, H. M., Wang, J. Q., Zhang, H. F. & Hu, G. D. (2019). *Intermetallics*, **104**, 143–153.
Xiao, D. & Gu, L. (2020). *Nano Select*, **1**, 183–199.
Xu, H. & Wu, P. (2022). *Natl Sci. Rev.* **9**, nwac045.
Xu, R., Yang, Y., Yin, F., Liu, P., Cloetens, P., Liu, Y., Lin, F. & Zhao, K. (2019). *J. Mech. Phys. Solids*, **129**, 160–183.
Yonekura, K., Maki-Yonekura, S. & Takaba, K. (2023). *Structure*, **31**, 1328–1334.
Zhang, C., Firestein, K. L., Fernando, J. F. S., Siriwardena, D., von Treifeldt, J. E. & Golberg, D. (2020). *Adv. Mater.* **32**, 1904094.
Zhang, C., Larionov, K. V., Firestein, K. L., Fernando, J. F. S., Lewis, C.-E., Sorokin, P. B. & Golberg, D. V. (2022). *Nano Lett.* **22**, 673–679.
Zhang, H., Zhang, T. & Zhang, X. (2023). *Adv. Sci.* **10**, 2300193.
Zhang, H.-T. & Zhang, X. (2022). *Mater. Res. Lett.* **10**, 1–5.
Zhang, Y., Xia, X., Ma, K., Xia, G., Wu, M., Cheung, Y. H., Yu, H., Zou, B., Zhang, X., Farha, O. K. & Xin, J. H. (2023). *Adv. Funct. Mater.* **33**, 2301607.
Zhao, B., Ngaloy, R., Ghosh, S., Ershadrad, S., Gupta, R., Ali, K., Hoque, A. M., Karpiak, B., Khokhriakov, D., Polley, C., Thiagarajan, B., Kalaboukhov, A., Svedlindh, P., Sanyal, B. & Dash, S. P. (2023). *Adv. Mater.* **35**, 2209113.
Zhao, S., Yang, Y. & Tang, Z. (2022). *Angew. Chem. Int. Ed.* **61**, e202110186.
Zheng, B., Lin, X., Zhang, X., Wu, D. & Matyjaszewski, K. (2020). *Adv. Funct. Mater.* **30**, 1907006.
Zhou, X., Falconer, J. L. & Medlin, J. W. (2022). *Microporous Mesoporous Mater.* **337**, 111913.